

Review

# On Manifestation of In-Medium Effects in Neutron Stars and Heavy-Ion Collisions

Dmitry N. Voskresensky <sup>1,2</sup>

<sup>1</sup> National Research Nuclear University (MEPhI), Kashirskoe shosse 31, 115409 Moscow, Russia; d.voskresen@gmail.com

<sup>2</sup> Joint Institute for Nuclear Research, RU-141980 Dubna, Moscow, Russia

Received: 27 November 2017; Accepted: 29 January 2018; Published: 8 February 2018

**Abstract:** This review focuses on the demonstration of an interrelation between various in-medium effects, which are manifested in the phenomena occurring in neutron stars and heavy-ion collisions. More specifically, the equation of state of a baryon-rich cold hadron matter is considered. It is done within the relativistic mean-field approach with  $\sigma$  field-scaled hadron masses and couplings, and a cut-mechanism is discussed leading to an increase of the stiffness of the dense baryon matter. Then, I discuss the role of the viscosity and thermal conductivity in description of the first-order phase transitions occurring in heavy-ion collisions and neutron stars. Next, the  $p$ -wave polarization effects on pion and kaon spectra are studied beyond the mean-field level. In particular, the pion softening effect is detailed. Then, a role of in-medium effects in neutrino radiation of neutron stars is discussed and effects of the bulk and shear viscosities in the problem of  $r$ -mode damping in young rapidly rotating pulsars are considered.

**Keywords:** neutron stars; heavy-ion collisions; in-medium effects

## 1. Introduction

Often, researchers studying heavy-ion collisions, where one deals with a non-equilibrium and a quasi-equilibrium hot and dense hadron matter, do not care about possible application of their models in other branches of nuclear physics, e.g., in neutron star physics, where one deals with the nuclear matter but in cold state, and, vice versa, the researchers considering neutron-star phenomena often ignore information known from heavy-ion-collision physics. The aim of this contribution is to partially overcome this gap demonstrating an interrelation between description of various phenomena in the heavy-ion-collision physics and the neutron-star physics. In the phenomena, which will be reviewed, the key role is played by in-medium effects in strongly-interacting nuclear matter.

## 2. EoS of Baryon-Rich Dense Not Too Hot Matter

### 2.1. Existing Constraints on EoS

Equation of state (EoS) of the cold hadronic matter should:

- satisfy experimental information on properties of dilute nuclear matter and not contradict the results of microscopical approaches like the Brueckner–Hartree–Fock (BHF) one;
- place empirical constraints on global characteristics of atomic nuclei [1];
- place constraints on the pressure of the nuclear matter from the description of particle transverse and elliptic flows and the  $K^+$  production in heavy-ion collisions, cf. [2,3];
- allow for the heaviest known compact stars [4];
- allow for an adequate description of the compact star cooling in the absence of the direct Urca (DU) neutrino processes in the majority of the known pulsars detected in soft X rays [1];

- and yield a mass–radius relation comparable with the empirical constraints including recent gravitation wave LIGO–Virgo detection [5];
- being extended to non-zero temperature  $T$  (for  $T < T_c$ , where  $T_c$  is the critical temperature of the deconfinement), appropriately describe supernova explosions, proto-neutron stars, and heavy-ion collision data [6,7], etc.

For more details, see discussion in [1,6–14].

Most difficult is the ability to satisfy simultaneously the heavy-ion-collision flow and the maximum neutron-star mass constraints. Flow of matter in heavy-ion-collision is directed both forward and perpendicular to the beam axis. At high densities, spectator nucleons may shield the transversal flow into their direction and generate an inhomogeneous density and pressure profile in the transversal plane. This effect is usually referred to as elliptic flow and depends on the EoS. An analysis of the nucleon flow data, which depends essentially only on the isospin-independent part of the EoS, was carried out in [2]. The flow constraint [2] to be fulfilled requires rather soft EoS of isospin-symmetric matter (ISM), whereas the EoS of the beta-equilibrium matter (BEM) should be stiff so that maximum available mass of the neutron star would be higher than the measured mass  $M = 2.01 \pm 0.04 M_\odot$  [4] of the pulsar PSR J0348+0432, being the heaviest at present. Various EoSs in comparison with the flow and neutron-star mass constraints are shown in Figure 1 taken from [1]. Models DD, D<sup>3</sup>C and DBHF (Bonn A) satisfy well the maximum neutron-star mass constraint but do not fulfill the flow constraint. On the contrary, the models NL $\rho$ , NL $\rho\delta$  satisfy the flow constraint but do not fulfill the maximum neutron-star mass constraint, and only models with  $\sigma$ -field-dependent effective hadron masses and couplings like KVR, KVOR, and the DD-F relativistic mean-field (RMF) model with density-dependent couplings are able to satisfy the flow constraint and marginally the maximum neutron-star mass constraint. However, hyperons and  $\Delta$  isobars are not incorporated within these models. Their inclusion additionally softens the EoSs [15–17] that may cause a problem with the fulfillment of the maximum neutron-star mass constraint. In conclusion, in-medium effects, e.g., those resulting in a modification of the hadron effective masses and couplings in matter, are required to fulfill both the flow and the maximum neutron-star mass constraints.

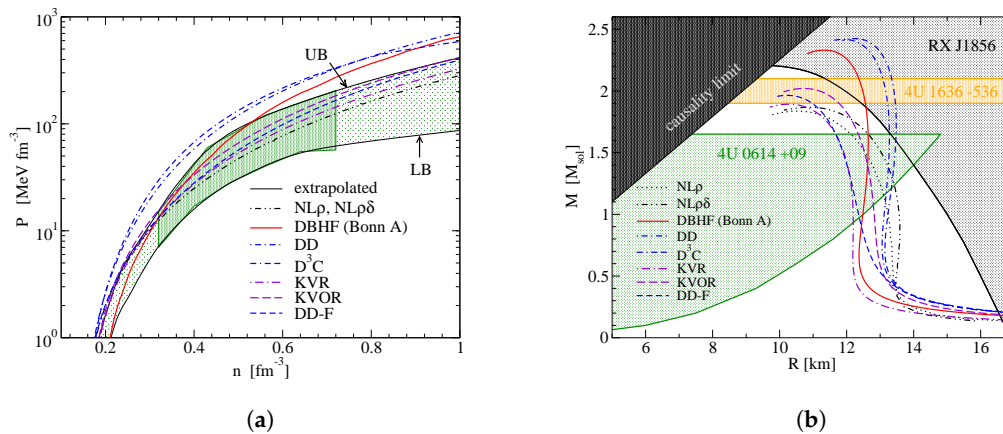


**Figure 1.** Figure is taken from [1]. (a) pressure region consistent with experimental flow data in ISM (dark shaded region). The light shaded region extrapolates this region to higher densities within an upper (UB) and lower (LB) borders; (b) mass–radius constraints from thermal radiation of the isolated neutron star RX J1856.5-3754 (grey hatched region) and from quasi-periodic oscillations (QPOs) in the Low-Mass X-Ray Binary (LMXB) 4U 0614+09 (green hatched area). The constraint from 4U 1636-536 (orange hatched region)  $2.0 \pm 0.1 M_\odot$  was withdrawn and should be replaced by a similar constraint  $2.01 \pm 0.04 M_\odot$  obtained later in [4] for PSR J0348+0432.

### 2.2. Cut-Mechanism for Stiffening of EoS

Ref. [12] studied various RMF models, where nucleons interact with scalar, vector and iso-vector mean fields and self- and cross- mean-field interaction terms might be also included. Usually, in such models, the magnitude of the scalar field increases monotonically with the nucleon density increase and the nucleon effective mass decreases. The latter quantity stops decreasing and the EoS stiffens, provided the mean-field self-interaction potential rises sharply in a narrow vicinity of the values of mean fields corresponding to nucleon densities  $n \gtrsim n_* > n_0$ , where  $n_0$  is the nuclear saturation density. Such a behaviour might be related to an excluded volume effect due to a strong repulsion at short distances between hadrons. As a result, the maximum neutron-star mass increases. Such a “cut”-procedure offered a simple way to stiffen the EoS at densities above  $n_*$  without altering it at  $n \lesssim n_0$ . The developed scheme allows an application to neutron stars of the RMF models, which are well fitted to finite nuclei but do not fulfill the experimental constraint on the maximum neutron-star mass. Then, the energy density is given by

$$\begin{aligned}
 E(n_p, n_n, f) &= E_{\text{kin}}(n_p, n_n, f) + E_V(n_p, n_n) + E_\sigma(f), \\
 E_{\text{kin}}(n_p, n_n, f) &= \left( \int_0^{p_{Fn}} + \int_0^{p_{Fp}} \right) \frac{p^2 dp}{\pi^2} \sqrt{p^2 + m_N^{*2}(f)}, \\
 E_V(n_p, n_n) &= \frac{C_\omega^2}{2m_N^2} (n_p + n_n)^2 + \frac{C_\rho^2}{8m_N^2} (n_p - n_n)^2, \\
 E_\sigma(f) &= \frac{m_N^4 f^2}{2C_\sigma^2} + U(f), \quad m_N^*(f) = m_N (1 - f).
 \end{aligned} \tag{1}$$

$C_j = g_{jN} m_N / m_j$ ,  $j = (\sigma, \omega, \rho)$  are fitting parameters of the RMF model,  $g_{jN}$  are meson-nucleon coupling constants,  $m_j$  are masses of  $j$ -hadrons,  $m_N$  is the nucleon mass,  $p_{Fn}$  and  $p_{Fp}$  are Fermi momenta of neutrons and protons,  $f = g_{\sigma N} \sigma / m_N$ ,  $U$  is the effective potential; in ordinary nonlinear Walecka (NLW) models, one chooses  $U(f) = m_N^4 (b f^3 / 3 + c f^4 / 4)$ , where  $b$  and  $c$  are fitting parameters. We also exploit a modified potential  $\tilde{U}$  depending on a  $c_\sigma$  parameter such that  $\tilde{U}$  undergoes a significant growth for  $f > f_{\text{cut}}$  (NLWcut model). The scalar field potential  $U(f)$  in the NLW model, and  $\tilde{U}(f)$  in the NLWcut model for various values  $c_\sigma$ , as functions of the scalar field parameter  $f$ , are shown in Figure 2a. The right panel demonstrates the nucleon effective mass in the ISM as a function of the nucleon density for the same models.

In the left panel in Figure 3, we show the pressure  $P$  for the NLW and NLWcut models under consideration as a function of the nucleon density in the ISM for various values  $c_\sigma$ , and the insertion demonstrates the binding energy per nucleon. The neutron-star mass and radius as functions of the central density for the same models are shown in the right panel. We see that the initial NLW model satisfies the flow constraint but does not fulfill the maximum neutron-star mass constraint, whereas two of four presented cut-versions of the model fulfill properly both constraints and one model fulfills the maximum neutron-star mass constraint marginally.

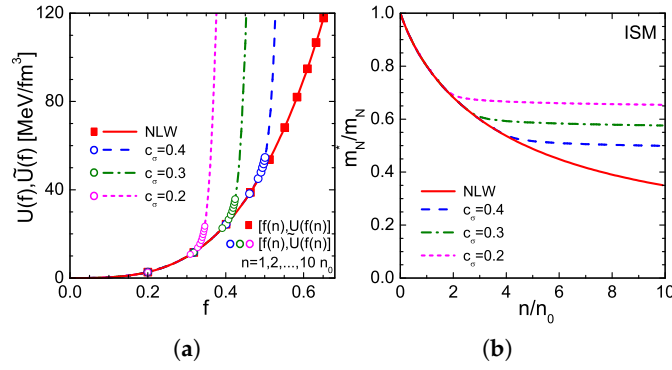


**Figure 2.** Figure from [12]. (a) the scalar field potential  $U(f)$  in the NLW model and  $\tilde{U}(f)$  in the NLWcut model for various values  $c_\sigma$ , as functions of the scalar field parameter  $f$ . The symbols indicate the values of  $[f(n); U(f(n)), \tilde{U}(f(n))]$  for the density  $n$  of the ISM varying from  $n_0$  to  $10n_0$  with the  $1n_0$  step; (b) the nucleon effective mass in the ISM as a function of the nucleon density for the same models.

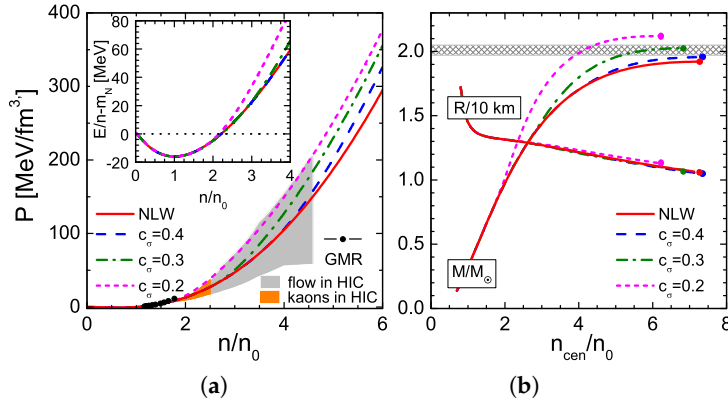


**Figure 3.** Figure from [12]. (a) total pressure  $P$  for the NLW and NLWcut models as a function of the nucleon density in the ISM for various values  $c_\sigma$ ; the insertion demonstrates the binding energy per nucleon. Two shadowed areas show the constraints on the pressure from the particle flow and the kaon production data in heavy-ion collisions extracted in [2,3]. Bold dots show the extrapolation of the pressure consistent with the giant monopole resonance (GMR) description [3]; (b) the neutron-star mass and radius as functions of the central density for models under consideration. The hatched band denotes the uncertainty in the value of the maximum measured neutron-star mass  $2.01 \pm 0.04 M_\odot$ .

### 2.3. Hyperon and $\Delta$ -Isobar Puzzles and Their Resolution in RMF Models with Scaled Hadron Masses and Couplings

In the standard RMF models, hyperons and  $\Delta$ -isobars may appear in neutron-star cores already for  $n \gtrsim (2-3)n_0$ , which results in a decrease of the maximum neutron-star mass below the observed limit. The problems were named the hyperon [15,16] and the  $\Delta$  [17,18] puzzles. These problems can be resolved in the RMF models with scaled hadron masses and couplings [9–11,14]. The model employed in [11,14] is a generalization of the NLW model with effective coupling constants  $g_{mb}^* = g_{mb}\chi_{mb}(\sigma)$  and hadron masses  $m_i^* = m_i\Phi_i(\sigma)$ , which are functions of the  $\sigma$  field [8],  $i = \{b, m\}$ , where  $m = \{\sigma, \omega, \rho, \phi\}$  lists the included mesonic fields,  $b = \{N, H, \Delta\}$  indicates a baryon (nucleon  $N = p, n$ ; hyperon  $H = \Lambda, \Sigma, \Xi$ ; and  $\Delta$  isobar). Quantities  $\chi_{mb}(\sigma)$  and  $\Phi_i(\sigma)$  are dimensionless scaling functions of the  $\sigma$  mean field. In the RMF approximation, the contribution of  $\Delta$ s to the energy density has the same form as for spin-1/2 fermions but with the spin degeneracy 4. With the standard solutions for the  $\omega$  and  $\rho$

meson mean fields, being expressed through baryon densities, the energy density of the model takes the following form

$$\begin{aligned}
 E[\{n_b\}, \{n_l\}, f] &= \sum_b E_{\text{kin}}(p_{F,b}, m_b \Phi_b(f), s_b) + \sum_{l=e,\mu} E_{\text{kin}}(p_{F,l}, m_l, s_l) \\
 &+ \frac{m_N^4 f^2}{2C_\sigma^2} \eta_\sigma(f) + \frac{1}{2m_N^2} \left[ \frac{C_\omega^2 n_V^2}{\eta_\omega(f)} + \frac{C_\rho^2 n_I^2}{\eta_\rho(f)} + \frac{C_\phi^2 n_S^2}{\eta_\phi(f)} \right], \\
 n_V &= \sum_b x_{\omega b} n_b, \quad n_I = \sum_b x_{\rho b} t_{3b} n_b, \quad n_S = \sum_H x_{\phi H} n_H,
 \end{aligned} \tag{2}$$

where we introduced the dimensionless scalar field  $f = g_{\sigma N} \chi_{\sigma N}(\sigma) \sigma / m_N$ , the coupling constant ratios  $x_{Mb} = g_{Mb} / g_{MN}$ ,  $M = \{\sigma, \omega, \rho\}$ ,  $x_{\phi H} = g_{\phi H} / g_{\omega N}$ ,  $g_{\phi N} = g_{\phi \Delta} = 0$ , and  $t_{3b}$  is the isospin projection of baryon  $b$ ; the Fermi momentum is related to the fermion density  $p_{F,j} = (6\pi^2 n_j / (2s_j + 1))^{1/3}$  with  $s_j$  standing for spin of fermion  $j = (b, l)$ ,  $l = (e, \mu)$ ;

$$C_M = \frac{g_{MN} m_N}{m_M}, \quad C_\phi = \frac{g_{\omega N} m_N}{m_\phi}. \tag{3}$$

The scaling functions are

$$\begin{aligned}
 \eta_\omega(f) &= \frac{\Phi_\omega^2(f)}{\chi_{\omega N}^2(f)}, \quad \eta_\rho(f) = \frac{\Phi_\rho^2(f)}{\chi_{\rho N}^2(f)}, \quad \eta_\phi(f) = \frac{\Phi_\phi^2(f)}{\chi_{\phi H}^2(f)}, \\
 \eta_\sigma(f) &= \frac{\Phi_\sigma^2[\sigma(f)]}{\chi_{\sigma N}^2[\sigma(f)]} + \frac{2C_\sigma^2}{m_N^4 f^2} U[\sigma(f)].
 \end{aligned}$$

As functions of  $f$ , they are constructed to fulfill all necessary constraints. The model uses universal mass scaling for nucleons and mesons,  $\Phi_N = \Phi_m = 1 - f$ , and universal scaling for coupling constants  $\chi_{\omega b}(f) = \chi_{\omega N}(f)$  and  $\chi_{\rho b}(f) = \chi_{\rho N}(f)$ , the coupling constant for  $\phi$  meson remains unscaled,  $\chi_{\phi H}(f) = 1$ , which results in the  $\phi$  scaling function  $\eta_\phi = (1 - f)^2$ . The scaling  $\eta_\sigma(f)$  includes also the scalar meson self-interaction potential  $U(\sigma)$ . The vector-meson coupling ratios with baryons  $x_{\omega B}$  and  $x_{\rho B}$  are chosen following the quark SU(6) symmetry. The baryon coupling ratios with the scalar field  $x_{\sigma B}$  are deduced from the potentials  $U_B(n_0) = C_\omega^2 m_N^{-2} x_{\omega B} n_0 - x_{\sigma B} (m_N + m_N \Phi_N(n_0))$  in ISM at the saturation baryon density  $n = n_0$ . There are large uncertainties in fixing of the  $\Delta$  potential  $U_\Delta(n_0) \equiv U_\Delta$  in the literature. The value  $U_\Delta = -50$  MeV, which results from calculations [19], is used as the most realistic choice but also a variation of  $U_\Delta$  is performed. The detailed description of parameters, which we use for all included baryon species, can be found in [11].

Refs. [9–11,14] use models of two kinds, the KVORcut-based models, where one exploits the cut in  $\omega$  sector choosing accordingly the  $\eta_\omega(f)$  dependence, and the MKVORcut-based models, where one exploits the cut in  $\rho$  sector choosing accordingly the  $\eta_\rho(f)$  dependence. In KVORcut models without inclusion of hyperons, the  $\rho^-$  condensate appears by the second-order phase transition and the influence of the  $\rho^-$  condensation on the EoS is minor. In MKVOR-based models, the  $\rho^-$  condensate (see in Section 2.4) appears by the first-order phase transition and the influence of the  $\rho^-$  condensation on the EoS is substantially stronger. In Figure 4, we show neutron-star masses as functions of the radii for MKVOR\*-based models [14]. In MKVOR\* models, we prevent the effective nucleon mass from vanishing at any density. In the MKVOR\* $\Delta$  model,  $\Delta$  isobars are included; in MKVOR\*H $\Delta\phi$  model hyperons,  $\Delta$ -isobars and  $\phi$ -mesons are included; in the model MKVOR\* $\Delta\rho$ ,  $\Delta$  and  $\rho^-$  condensate are included; and in MKVOR\*H $\Delta\phi\rho$  model hyperons,  $\Delta$ ,  $\phi$  and  $\rho^-$  are included, respectively. As we see, in the presence of  $\Delta$ -isobars, the  $\rho^-$  condensate softens EoS substantially, but, even with its inclusion, we are able to satisfy the maximum neutron-star mass constraint.

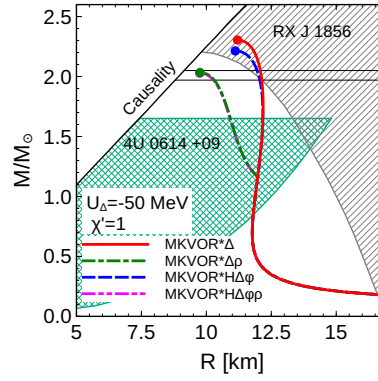


**Figure 4.** Neutron star masses versus radii for MKVOR\* $\Delta$ , MKVOR\*H $\Delta\phi$ , MKVOR\* $\Delta\rho$ , MKVOR\*H $\Delta\phi\rho$  models.

#### 2.4. Charged $\rho$ Condensation

The non-Abelian  $\rho$  meson field is analogous to the massive gluon field. Ref. [20] demonstrated that, in a dense nucleon isospin-asymmetric matter at an appropriate decrease of the effective  $\rho$  meson mass, there may occur a charged  $\rho$  condensation. Then, the phenomenon of the charged  $\rho^-$  condensation was incorporated in the RMF models with scaled hadron masses and coupling constants in [8]. Similarly, the charged  $\rho^-$  condensation may appear in very strong magnetic fields [21,22].

The contribution of the charged  $\rho^-$  meson condensate to the energy density is then given by [14]

$$\Delta E_{\text{ch},\rho}[\{n_b\};f] = -\frac{C_\rho^2}{2m_N^2\eta_\rho}(n_I + n_\rho)^2\theta(-n_I - n_\rho) - \mu_{\text{ch},\rho}n_{\text{ch},\rho}, \quad (4)$$

where  $\theta(-n_I - n_\rho) = 1$  for  $n_I + n_\rho < 0$  and zero otherwise. The solution for  $n_I + n_\rho < 0$  corresponds to  $\rho_0^{(3)} = \frac{\mu_{\text{ch},\rho} - m_\rho\Phi_\rho}{g_\rho\chi'_\rho}$ ,  $|\rho_c|^2 = \frac{(-n_I - n_\rho)\theta(-n_I - n_\rho)}{2m_\rho\eta_\rho^{1/2}\chi'_\rho}$ , where  $n_\rho = a(m_\rho\Phi_\rho - \mu_{\text{ch},\rho})$ ,  $a = \frac{m_N^2\eta_\rho^{1/2}\Phi_\rho}{C_\rho^2\chi'_\rho}$ . The  $\rho$  charged density is  $n_{\text{ch},\rho} = -2m_\rho\Phi_\rho(f)|\rho_c|^2 < 0$ . The scaling of the non-abelian  $\rho - \rho$  interaction  $\chi'_\rho$  is put unity.

### 3. Viscosity and Thermal Conductivity Effects at First-Order Phase Transitions in Heavy-Ion Collisions and Neutron Stars

#### 3.1. Pressure–Baryon Density Behavior at First-Order Phase Transitions

At various first-order phase transitions, the pressure–density behaviour gets a van der Waals form. It occurs for the nuclear liquid–vapor phase transition, whose signatures are manifested in low-energy heavy-ion collisions, and might be for quark–hadron phase transition in baryon-rich matter, for phase transitions to the pion- and kaon- and charged  $\rho$ -condensate states in rather massive neutron stars and might be for nucleon- $\Delta$ -resonance state transition in ISM, as follows in some models (cf. Figure 6, which will be demonstrated and discussed below).

In Figure 5, we show typical behaviour of the pressure isotherms as functions of the density at the first-order liquid–vapor-like phase transition. The horizontal dashed line shows the Maxwell construction (MC). At equilibrium, the chemical potentials  $\mu_A = \mu_D$ . The interval AB corresponds to a metastable supercooled vapor (SV) and the interval CD, to a metastable overheated liquid (OL). The interval BC corresponds to an unstable spinodal region.

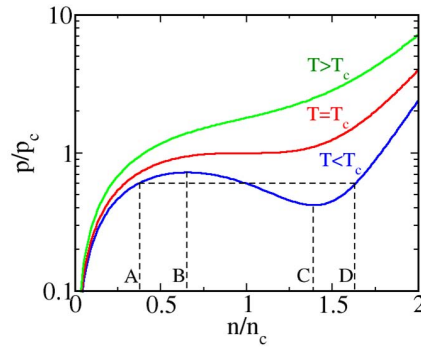


**Figure 5.** Schematic pressure isotherms as functions of the density at a liquid–vapor-like phase transition.  $P_c$ ,  $n_c$  and  $T_c$  are the pressure, density and temperature at the critical point.

Calculations [11] show that, with increase of the baryon density in the cold ISM, there may appear a phase transition to the  $\Delta$ -rich matter. Pressures as functions of the density in the ISM for MKVOR\* model and MKVOR\* $\Delta$  model are shown in Figure 6. As is seen, for the values of the  $\Delta$  optical potential  $U_\Delta(n = n_0) > -56$  MeV, the transition proves to be of the second-order and, for  $U_\Delta(n = n_0) < -56$  MeV, it is of the first-order. Although the most realistic value for the  $\Delta$  optical potential is estimated as  $U_\Delta(n = n_0) \sim -50$  MeV, a variation is allowed. In the case of the first-order phase transition, the pressure isotherms as functions of the baryon density demonstrate a back-bending. There are two narrow spinodal regions. A specifics of the back-bending is described in [11]. Note that the flow constraint [2] is better fulfilled in the presence of the first-order transition to the  $\Delta$ -rich matter. A first-order phase transition into a  $\Delta$ -rich state that we obtained within the MKVOR\* $\Delta$  model for  $U_\Delta < -56$  MeV could manifest itself in an increase of the pion yield at typical energies and momenta corresponding to the  $\Delta \rightarrow \pi N$  decays in heavy-ion collision experiments.

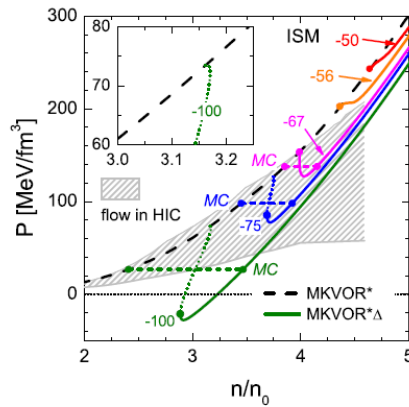


**Figure 6.** Figure from [11]. Pressure as a function of the density in the ISM for MKVOR\* model (dashed line) and MKVOR\* $\Delta$  model (dotted and solid lines). The hatched region indicates the nucleon flow constraint [2] in heavy-ion collisions. MC lines indicate the Maxwell construction.

In neutron stars, appearance of a strong phase transition may result in a second neutrino burst if the transition occurred right after supernova explosion and a hot neutron star formation. A possibility of the delayed second neutrino burst in SN 1987A event has been considered in [23–25]. It might be associated with a significant delay of the heat transport to the neutron-star surface if the system is close to the pion–condensate phase transition. Recently, new arguments have been expressed for that namely two neutrino bursts were measured during 1987A explosion, one delayed respectively the other one by 4.7 h, cf. [26]. The second burst could then be related to the phase transition of the neutron star to the pion condensate state. In addition, a phase transition to the pion- or to the kaon–condensate state could

occur during 10-s-period of the neutron star formation. Moreover, the first-order phase transition, if it occurs, could result in a blowing off a star matter. In old neutron stars, the first-order phase transition, if it occurs, could result in a strong star-quake [25,27].

### 3.2. Hydrodynamical Description

Here, we follow the analysis of works [28–31]. Assume that a nuclear system is rather close to a critical point of a liquid–vapor-type first-order phase transition. Then, the velocity of a fluctuation (seed),  $\vec{u}$ , is much less than the mean thermal velocity and we may use equations of non-relativistic non-ideal hydrodynamics: the Navier–Stokes equation, the continuity equation, and equation for the heat transport:

$$m^*n [\partial_t u_i + (\vec{u}\nabla)u_i] = -\nabla_i P + \nabla_k \left[ \eta \left( \nabla_k u_i + \nabla_i u_k - \frac{2}{d} \delta_{ik} \text{div} \vec{u} \right) + \zeta \delta_{ik} \text{div} \vec{u} \right], \quad (5)$$

$$\partial_t n + \text{div}(n\vec{u}) = 0, \quad (6)$$

$$T \left[ \frac{\partial s}{\partial t} + \text{div}(s\vec{u}) \right] = \text{div}(\kappa \nabla T) + \eta \left( \nabla_k u_i + \nabla_i u_k - \frac{2}{d} \delta_{ik} \text{div} \vec{u} \right)^2 + \zeta (\text{div} \vec{u})^2. \quad (7)$$

$n$  is the density of the conserving charge (here, the baryon density),  $m^*$  is the effective baryon mass,  $P$  is the pressure,  $\eta$  and  $\zeta$  are the shear and bulk viscosities,  $d$  shows the geometry of the fluctuation (droplets, rods, slabs),  $T$  is the temperature,  $s$  is the entropy density, and  $\kappa$  is the thermal conductivity.

As an example, we consider a van der Waals fluid. Then, adiabatic trajectories,  $\tilde{s} \equiv s/n \simeq \text{const}$ , for an expansion of a uniform fireball to vacuum, are shown in Figure 7. The SV and the OL regions are between the MC and the isothermal spinodal (ITS) curves, on the left and on the right, respectively. The adiabatic spinodal (AS) curve bounds the AS region from above. For  $\tilde{s}_{cr} > \tilde{s} > \tilde{s}_{MC2}$ , where  $\tilde{s}_{cr}$  corresponds to the value of the specific entropy  $\tilde{s}$  at the critical point and the line with  $\tilde{s}_{MC2}$  passes through the point  $n/n_{cr} = 3$  at  $T = 0$ , the system traverses the OL state (the region OL in Figure 7), the ITS region (below the ITS line) and the AS region (below the AS line). For  $\tilde{s} > \tilde{s}_{cr}$ , the system trajectory passes through the SV state (the region SV in Figure 7) and the ITS region.

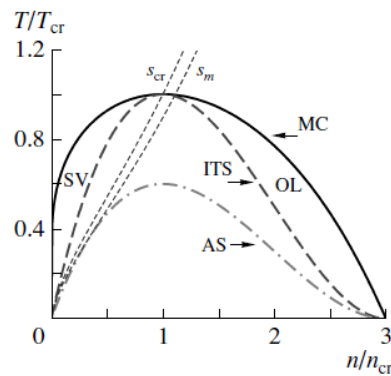


**Figure 7.** Figure from [31]. The phase diagram of the van der Waals EoS,  $T(n)$ -plane. The bold solid, dashed and dash-dotted curves demonstrate the boundaries of the MC, the spinodal region at  $T = \text{const}$  and  $\tilde{s} = \text{const}$ , respectively. The short dashed lines show adiabatic trajectories of the system evolution: the curve labeled  $s_{cr}$  passes through the critical point;  $s_m$ , through the maximum pressure point  $P(n_{P,max})$  on the  $P(n)$  plane.

Note that for the quark–hadron first-order phase transition the phase diagram looks a bit different since then  $T_c$  increases with a decrease of the baryon density [32,33]. However presence of this peculiarity does not change our general analysis given here.



Note that, for the hadron–quark transition in heavy-ion collisions, besides a possibility of the first-order phase transition, one also discusses a possibility of the crossover. The latter transition is expected at collision energies achievable at RHIC (Brookhaven) and LHC (CERN). Lattice calculations performed for a baryon-less matter also indicate on the crossover transition. For lower collision energies relevant for NICA (Dubna) and FAIR (Darmstadt) facilities, one expects to find signatures of the first-order phase transition. Although it is not excluded that even in the NICA-FAIR range of the collision energies the hadron–quark transition is the crossover, in this review, I focus only on the description of the signatures of the first-order phase transition.

All thermodynamic quantities can be expanded near an arbitrary reference point  $(n_r, T_r)$ , or  $(n_r, \tilde{s}_r)$ , which we assume to be close to the critical point. The Landau free energy in the variables  $\delta n = n - n_{cr}$ ,  $\delta T = T - T_{cr}$ ,  $\delta(\delta F_L)/\delta(\delta n) = P - P_f + P_{MC}$  is as follows:

$$\delta F_L = \int \frac{d^3x}{n_{cr}} \left\{ \frac{cm^*[\nabla(\delta n)]^2}{2} + \frac{\lambda m^{*3}(\delta n)^4}{4} - \frac{\lambda v^2 m^*(\delta n)^2}{2} - \epsilon \delta n \right\}, \quad (8)$$

where  $\epsilon = P_f - P_{MC}$  is expressed through the pressure at the MC. The maximum of the quantity  $\epsilon$  is  $\epsilon^m = 4\lambda v^3/(3\sqrt{3})$ . The first term in Equation (8) is due to the surface tension,  $\delta F_{L,\text{surf}} = \sigma S$ ,  $S$  is the surface of the seed. For the van der Waals equation of state:

$$v^2(T) = -4 \frac{\delta T n_{cr}^2 m^{*2}}{T_{cr}}, \quad \sigma = \sigma_0 \frac{|\delta T|^{3/2}}{T_{cr}^{3/2}}, \quad \sigma_0 = 32m^* n_{cr}^2 T_{cr} c. \quad (9)$$

Using Equation (6), and keeping only linear terms in  $u$ , since near the critical point processes develop slowly,  $v^2 \propto -\delta T$ , we rewrite Equation (5) in the dimensionless variables  $\delta\rho = v\psi$ ,  $\xi_i = x_i/l$ ,  $i = 1, \dots, d$ ,  $d = 3$  for seeds of spherical geometry,  $\tau = t/t_0$  as

$$\begin{aligned} -\beta \frac{\partial^2 \psi}{\partial \tau^2} &= \Delta_{\tilde{\xi}} \left( \Delta_{\tilde{\xi}} \psi + 2\psi(1 - \psi^2) + \tilde{\epsilon} - \frac{\partial \psi}{\partial \tau} \right), \\ l &= \left( \frac{2c}{\lambda v^2} \right)^{1/2}, \quad t_0 = \frac{2(\tilde{d}\eta_r + \zeta_r)}{\lambda v^2 n_{cr} m_{cr}^*}, \quad \tilde{\epsilon} = \frac{2\epsilon}{\lambda v^3}, \quad \beta = \frac{cn_{cr}^2 m_{cr}^{*2}}{(\tilde{d}\eta_r + \zeta_r)^2}, \end{aligned} \quad (10)$$

and  $\tilde{d} = 2(d-1)/d$ . One often speculates about a manifestation of fluctuations as a measure of the closeness to the critical quark–hadron first-order phase transition point in the course of heavy-ion collisions. As we demonstrate, processes near the critical point are frozen (critical slowing down). Thereby, at least a region very close to the critical point can hardly be manifested via abnormal fluctuations in the course of heavy-ion collisions since these fluctuations do not have enough time to develop.

Equation (10) is supplemented by Equation (7) for the heat transport, which owing to Equation (6) after linearization simplifies to

$$T_{cr} \left[ \partial_t \delta s - s_{cr}(n_{cr})^{-1} \partial_t \delta n \right] = \kappa_r \Delta \delta T. \quad (11)$$

The variation of the temperature is related to the variation of the entropy density  $s[n, T]$  by  $\delta T \simeq T_{cr}(c_{V,r})^{-1} (\delta s - (\partial s / \partial n)_{T,cr} \delta n)$ . Note that the reference point differs from the critical point, although we take the reference point in the vicinity of the critical point. This circumstance is important for the determination of the specific heat density  $c_{V,r}$  and transport coefficients, whereas other quantities are already smooth functions of  $n, T$ .

Equation (10) differs from the standard Ginzburg–Landau equation exploited in condensed matter theory. The difference disappears, if one puts the bracket-term in the r.h.s. of Equation (10) to zero. This procedure is not legitimate for consideration of fluctuations at a short time. Thereby,

there exists an initial stage of the dynamics of seeds ( $t \lesssim t_{\text{init}}$ ), which is not described by the standard Ginzburg–Landau equation [28,29].

The time scale for the relaxation of the density following Equation (10) is  $t_\rho \propto R$ , where  $R$  is the size of a seed (after awhile, an overcritical seed begins to grow with a constant velocity already following the standard Ginzburg–Landau equation), and the time scale for the relaxation of the entropy/temperature, following Equation (11), is

$$t_T = R^2 c_{V,r} / \kappa_r \propto R^2. \tag{12}$$

The evolution of a seed is governed by the slowest mode. Thus, for  $t_T(R) < t_\rho(R)$ , i.e., for  $R < R_{\text{fog}}$  ( $R_{\text{fog}}$  is the typical size of the seed at which  $t_\rho = t_T$ ), dynamics of seeds is controlled by Equation (10) for the density mode. For seeds with sizes  $R > R_{\text{fog}}$ ,  $t_T \propto R^2$  exceeds  $t_\rho \propto R$  and growth of seeds is slowed down. Thereby, the number of seeds with the size  $R \sim R_{\text{fog}}$  may increase with time. For the quark–hadron phase transition  $R_{\text{fog}} \sim 0.1\text{--}1$  fm and for the nuclear liquid–vapor transition  $R_{\text{fog}} \sim 1\text{--}10$  fm  $\lesssim R_{\text{fb}}(t_{f.o.})$ , where  $R_{\text{fb}}(t_{f.o.})$  is the fireball size at the freeze out,  $t_{f.o.}$  is the fireball evolution time till freeze out. Thus, thermal conductivity effects may manifest themselves in heavy-ion collision dynamics.

There are only two dimensionless parameters in Equation (10),  $\tilde{\epsilon}$  and  $\beta$ . The parameter  $\tilde{\epsilon}$  is responsible for a difference between the Landau free energies of the metastable and stable states. For  $t_\rho \gg t_T$  (isothermal stage),  $\tilde{\epsilon} \simeq \text{const}$  and dependence on this quantity disappears because of  $\Delta\zeta\tilde{\epsilon} \simeq 0$ . Then, dynamics is controlled by the parameter  $\beta$ , which characterizes an inertia. It is expressed in terms of the surface tension and the viscosity as

$$\beta = (32T_{cr})^{-1} [\tilde{d}\eta_r + \zeta_r]^{-2} \sigma_0^2 m^*. \tag{13}$$

The larger is the viscosity and the smaller is the surface tension, the effectively more viscous (inertial) is the fluidity of seeds. For  $\beta \ll 1$ , one deals with the regime of effectively viscous fluid and at  $\beta \gg 1$ , with the regime of perfect fluid, for the nuclear liquid–vapor phase transition typically  $\beta \sim 0.01$ , and for the quark–hadron phase transition  $\beta \sim 0.02\text{--}0.2$ , even for very low value of the ratio  $\eta/s \simeq 1/(4\pi)$ . The latter quantity characterizes fluidity ultra-relativistic systems where viscosity proves to be very small but finite [34]. In the case of baryon-rich matter, one deals with effectively very viscous fluidity of density fluctuations in both nuclear liquid–vapor and quark–hadron phase transitions. An interplay between viscosity, surface tension, and thermal conductivity effects is responsible for the typical size of the fluctuations.

In neutron stars, an overcritical pion–condensate drop reaches a size  $R \sim 0.1$  km for  $t \sim 10^{-3}$  s by the growth of the density mode. Then, it may reach  $R \sim (1\text{--}10)$  km for  $t \sim 10$  s up to several hours (rather than for typical collapse time  $\sim 10^{-3}$  s) with a delay owing to neutrino heat transport to the surface (effect of thermal conductivity) that strongly depends on the value of the pion softening (see in the next section), which is stronger for most massive neutron stars, cf. [23–25]. In addition, the dynamics of the pion–condensate transition is specific since it occurs in inhomogeneous state,  $\vec{k} \neq 0$ . The seeds of the liquid-crystal-like state are elongated in the process of their growth [35], and such an effect is observed in liquid crystals.

It is well known that at, least in the mean-field approximation, the ITS line and AS line are different. From the exact thermodynamic relation, one gets

$$u_s^2 = u_T^2 + \frac{T}{nm^*c_V} \left[ \left( \frac{\partial P}{\partial T} \right)_n \right]^2.$$

The variable  $u_s, u_s^2 = m^{-1}(\partial P/\partial n)_s$  has the meaning of the adiabatic sound velocity (at  $\tilde{s} = \text{const}$ ) and  $u_T, u_T^2 = m^{-1}(\partial P/\partial n)_T$  of the isothermal sound velocity (at  $T = \text{const}$ ). The former quantity characterizes propagation of sound waves in ideal hydrodynamics. In non-ideal hydrodynamics at

finite values of the thermal conductivity,  $\kappa$ , the propagation of sound waves is defined by the interplay between  $u_T$  and  $u_s$ . The conditions  $u_T = 0$  and  $u_s = 0$  define on a  $T(n)$  plane the ITS line and AS line. The maximum temperature points on these lines are the critical temperature  $T_{cr}$  (on ITS line) and the adiabatic maximum temperature  $T_{P,max}$  (on AS line). In the mean-field approximation,  $c_V$  has finite non-negative values. Therefore,  $u_T^2 \leq 0$  on the AS line ( $u_s = 0$ ). Note that, as we have mentioned, even in the region near the critical point, where thermodynamic fluctuations are strong (fluctuation region), a mean-field treatment can be applied in dynamics, since the system spends in this region a shorter time than the time needed for a development of the critical fluctuations. Calculations performed in mean-field models show that  $T_{cr}$  is significantly higher than  $T_{P,max}$ , e.g., within the Nambu-Jona-Lasinio (NJL) model, one obtains  $T_{P,max} \sim T_{cr}/2 \simeq 45$  MeV for the chiral transition. At such small temperatures as  $T_{P,max}$ , the chiral and deconfinement transitions are unlikely in heavy-ion collisions.

To find onset of instabilities, consider dynamic variables  $a = (n, s, T)$  to be modulated as  $\delta a = \delta a_0 \exp[\gamma t + i\vec{p}\vec{r}]$ . For  $p \ll p_T$ , where  $p_T$  is the mean thermal momentum, from the linearized equations of non-ideal hydrodynamics, one may find the increment  $\gamma(p)$ ,

$$\gamma^2 = -p^2 \left[ u_T^2 + \frac{(\frac{4}{3}\eta + \zeta)\gamma}{m^*n} + cp^2 + \frac{u_s^2 - u_T^2}{1 + \frac{\kappa p^2}{(c_V\gamma)}} \right].$$

The solutions are two density modes (existing even in the limit  $\kappa = 0$ ) and one thermal mode (existing only for  $\kappa \neq 0$ ).

For the limiting case of zero shear and bulk viscosities and non-zero, but small thermal conductivity, for  $-u_T^2 \ll 1$ , i.e., slightly below the ITS line, for the most rapidly growing mode  $\gamma = \gamma_m$ ,  $p = p_m \ll p_T$ , one gets

$$\gamma_m \simeq \frac{\kappa u_T^4}{4cc_V u_s^2}, \quad p_m^2 \simeq -u_T^2/(2c).$$

For any small but finite value  $\kappa$ , the solution  $\gamma_m$  results in instability already for  $u_T^2 < 0$  (i.e., below the ITS line). On the contrary, in case  $\kappa = \eta = \zeta = 0$ , i.e., within ideal hydrodynamics, the instability appears, when the system trajectory crosses the AS line rather than the ITS line. Since, in reality  $\kappa \neq 0$ , it is possible to conclude that the instability condition  $u_s^2 < 0$  should be replaced in favor of  $u_T^2 < 0$ . For large values of  $\kappa$ , the density mode proves to be the most rapidly growing one, but the condition for the onset of instability,  $u_T^2 = 0$ , is not changed. For  $\beta \ll 1$  (e.g. for a large viscosity), we get

$$\gamma_m \simeq \frac{-u_T^2 m^* n_{cr}}{4\eta/3 + \zeta}, \quad p_m^2 \simeq -u_T^2 \sqrt{\beta}/c.$$

Note that in condensed matter physics a transition from a liquid to a glass state can be interpreted as a first-order phase transition occurring within a spinodal region at a very high viscosity [35]. Then, there appears an order at several Å-scale, which transforms in a disorder at larger distances.

According to our findings, spinodal instabilities may manifest themselves in experiments with heavy ions in some collision energy interval that corresponds to the first-order phase transition region of the QCD phase diagram. One of the possible signatures is a manifestation of fluctuations with a typical size  $r \sim 1/p_m$  in the rapidity spectra (see details in Ref. [30]). In conclusion, we note that viscosity and thermal conductivity are driving forces of the first-order liquid–vapor and quark–gluon phase transitions and the spinodal instability occurs for  $T$  below the ITS line.

The above considered are the first-order phase transitions of the liquid–vapor type when there exists only one conserved charge, as the baryon number in heavy-ion collisions. In BEM of neutron stars, there are two conserved charges, the baryon and the lepton ones. In this case, the equilibrium configuration is a mixed pasta phase [36], which appears provided a surface tension is below a critical value  $\sigma_c$ , cf. [37]. Finite-size screening effects prove to be very important [38]. They were studied on

examples of the quark–hadron first-order phase transition [38,39] and the kaon–condensate phase transition [40]. For the quark–hadron first-phase transition,  $\sigma_c \sim 60 \text{ MeV}/\text{fm}^2$ . It was shown that, in both cases, the  $P(n)$  behaviour is close to that given by the MC. In [41], the finite-size effects in the nuclear pasta phase in the inner neutron-star crust have been considered.

#### 4. Pions and Kaons in Dense Baryon Matter

We treated nuclear systems on the mean-field level above. Pions and kaons are pseudoscalar Goldstone-like particles and they do not contribute to EoS on the mean-field level. For their description, medium-polarization effects are important. Different processes involved in nuclear phenomena occurring on the hadron level are characterized by various energy-momentum and time-length scales. Of the order of the confinement radius  $r_\Lambda$  are scales associated with masses of heavy mesons such as  $\sigma$ ,  $\omega$  and  $\rho$  ( $r \sim r_\sigma \sim 1/m_\sigma$ ,  $r \sim r_\omega \sim 1/m_\omega$ ,  $r \sim r_\rho \sim 1/m_\rho$ ) and with nucleons,  $r_N \sim 1/m_N$ . In description of in-medium pions and kaons at  $n \lesssim$  several  $n_0$ ,  $T \lesssim 100 \text{ MeV}$ , we treat these scales as short-ranged. Typical low momenta are  $k \sim m_\pi$  and  $k \sim p_F \sim 1/(2 m_\pi)$ , where  $m_\pi \simeq 140 \text{ MeV}$  is the pion mass and  $p_F$  is the Fermi momentum of the nucleon, which corresponds to the length scales  $r \sim 1/m_\pi$  and  $r \sim 1/p_F$ , respectively. These latter scales are treated as long-ranged microscopic scales. Time scales that correspond to low energies are  $\sim 1/\epsilon_F$  ( $\epsilon_F$  is the Fermi energy of nucleons  $\simeq 40 \text{ MeV}$  in ISM for  $n = n_0$ ),  $\sim 1/m_\pi$  and  $\sim 1/\omega_\Delta$  ( $\omega_\Delta = m_\Delta - m_N \simeq 2.1 m_\pi$  is the energy gap for the excitation of  $\Delta$  isobars). Minimal energy scale of our interest is  $\tilde{\omega}(n)$ , where  $\tilde{\omega} \leq m_\pi$  is an effective pion gap (see Figure 9 below). This energy scale arises due to a collective pion softening effect appearing for nucleon densities  $n > n_c^{(1)} \simeq (0.5\text{--}0.8) n_0$ , cf. [25,42].

Consider the Fermi-liquid approach with the explicit incorporation of the in-medium pion exchange. For zero temperature, it was formulated by A. B. Migdal in Ref. [43], and, then, the approach was generalized for finite temperatures and non-equilibrium systems, cf. [25,42,44,45]. Within this approach, the long-range processes are treated explicitly, whereas short-range processes are described by local quantities approximated by phenomenological, so-called Landau–Migdal, parameters. At low excitation energies, the retarded  $NN$  interaction amplitude is presented as follows:

$$\text{Diagram 1} = \text{Diagram 2} + \text{Diagram 3} + \text{Diagram 4}, \tag{14}$$

where

$$\text{Diagram 5} = \text{Diagram 6} + \text{Diagram 7}. \tag{15}$$

The solid line stands for a nucleon, the double-line, for a  $\Delta$  isobar. At a higher temperature, the  $\Delta\Delta^{-1}$  diagrams should be included [44]. The doubly-dashed line corresponds to the exchange of the free pion with inclusion of the contributions of the residual s-wave  $\pi NN$  interaction and  $\pi\pi$  scattering, i.e., the residual irreducible interaction to the nucleon particle-hole and delta-nucleon hole insertions. The empty block in Equation (15) is irreducible with respect to the particle-hole, delta-nucleon hole and pion states and is thereby essentially more local than contributions given by explicitly presented graphs. It is given by

$$\Gamma_{\vec{n}\alpha\beta,\vec{n}'\gamma\delta}^\omega = F_{\vec{n},\vec{n}'} \delta_{\alpha\beta} \delta_{\gamma\delta} + G_{\vec{n},\vec{n}'} \vec{\sigma}_{\alpha\beta} \vec{\sigma}_{\gamma\delta}, \tag{16}$$

where  $\vec{\sigma}$  is the Pauli matrix,  $F$  and  $G$  are functions dependent on the direction of the momenta of incoming and outgoing nucleon and hole at the Fermi surface. One introduces the dimensionless amplitudes  $f_{\vec{n},\vec{n}'} = C_0^{-1} F_{\vec{n},\vec{n}'}$  and  $g_{\vec{n},\vec{n}'} = C_0^{-1} G_{\vec{n},\vec{n}'}$  where  $C_0^{-1} = m_N^*(n_0) p_F(n_0) / \pi^2$  is the density of states at the Fermi surface for  $n = n_0$ . The amplitudes  $f_{\vec{p},\vec{p}'}$  and  $g_{\vec{p},\vec{p}'}$  are then expanded in the Legendre polynomials with the coefficients known as Landau–Migdal parameters. In most cases, it is sufficient

to deal with zero and first harmonics. These harmonics can be extracted from comparison with the data or can be computed within some models.

The irreducible part of the interaction involving  $\Delta$  isobar is constructed similarly to Equation (15). The main part of the  $N\Delta$  interaction is due to the pion exchange. Although information on the local part of the  $N\Delta$  interaction is scarce, one concludes [25] that the corresponding Landau–Migdal parameters are essentially smaller than those for  $NN$  interaction. Therefore, and also for the sake of simplicity, we neglect this term.

The spectrum of the particle excitations is determined by the spectral function given by the imaginary part of the retarded Green function  $A = -2\text{Im}G^R$ . Resummation of diagrams shown in Equation (14) yields the following Dyson equation for the retarded pion Green function  $G^R$  and self-energy  $\Sigma^R$ ,

$$\text{---} = \text{---} + \text{---} \text{---} + \text{---} \text{---} + \text{---} \Sigma_{res}^R \text{---} \text{---} \tag{17}$$

Here,  $\Sigma_{res}^R$  is a residual retarded pion self-energy that includes the contribution of all diagrams, which are not presented explicitly in Equation (17), like the  $s$ -wave  $\pi N$  and  $\pi\pi$  scattering (included by doubly-dashed line in Equation (15)). The full vertex takes into account  $NN$  correlations

$$\text{---} \text{---} = \text{---} \text{---} + \text{---} \text{---} \text{---} \tag{18}$$

Resummation of Equation (14) yields in the spin-isospin channel

$$\text{---} \text{---} = \left[ \frac{C_0 g'}{1 - C_0 g'} + \text{---} \right] (\vec{\tau}_1 \vec{\tau}_2) (\vec{\sigma}_1 \vec{\sigma}_2) \tag{19}$$

The total resummed  $NN$  interaction reads

$$\Gamma_{NN}^R = C_0 [F + F' \vec{\tau}_1 \vec{\tau}_2 + (G + G' \vec{\tau}_1 \vec{\tau}_2) \vec{\sigma}_1 \vec{\sigma}_2] + f_{\pi NN}^2 T_\pi \vec{\sigma}_1 \vec{k} \cdot \vec{\sigma}_2 \vec{k}, \tag{20}$$

and  $f_{\pi NN} \simeq 1/m_\pi$  is the pion–nucleon  $P$ -wave coupling. First, three square-bracketed terms of Equation (20) arise due to the loop-resummation of the empty block graphs in Equation (15), whereas the last term of Equation (20) is due to the contribution of the second diagram of Equation (15). Amplitudes  $F, F', G, G'$ , and  $T_\pi$  are expressed with the help of the dimensionless Landau–Migdal parameters  $f, f', g, g'$ , related to the local  $NN$ -interaction in the particle-hole channel

$$\begin{aligned} F &= f\Gamma(f), \quad F' = f'\Gamma(f'), \\ G &= g\Gamma(g), \quad G' = g'\Gamma(g'), \\ T_\pi &= \Gamma^2(g')G_\pi^R(\omega, k) = \Gamma^2(g')/[\omega^2 - m_\pi^2 - k^2 - \Sigma^R(\omega, k)]. \end{aligned} \tag{21}$$

The Landau–Migdal parameters  $f = (f_{nn} + f_{np})/2, f' = (f_{nn} - f_{np})/2$  in the scalar channel are expressed via the nucleon incompressibility and can be calculated already on the mean-field level, cf. [10,46]. Calculation of the spin-parameters  $g = (g_{nn} + g_{np})/2, g' = (g_{nn} - g_{np})/2$  needs to incorporate the contribution in the  $NN$  interaction beyond the mean-field Hartree-level.

For small energies  $\omega \ll m_\pi$  and for momenta  $k \lesssim p_F$ , expression for  $\Gamma(x)$ , where  $x = f, f', g, g'$ , simplifies, since at such energies the  $\Delta$  – nucleon hole ( $\Delta N^{-1}$ ) contribution in Equation (17) is a smooth function of  $\omega$  and  $k$ , and, doing particle–hole resummation, one can explicitly take into account only the  $NN^{-1}$  loop. Then,

$$\Gamma(x) \simeq 1 / [1 + 2xp_F/p_F(n_0)] \tag{22}$$

There were found two sets of the parameters fitted to atomic-nucleus experiments, cf. [47], being  $f \simeq 0.25$ ,  $f' \simeq 1$ ,  $g \simeq 0.5$ ,  $g' \simeq 1$  and  $f \simeq 0$ ,  $f' \simeq 0.5\text{--}0.6$ ,  $g \simeq 0.05 \pm 0.1$ ,  $g' \simeq 1.1 \pm 0.1$ . Uncertainties in numerical values appear due to attempts to get the best fit to experimental data in each specific case modifying the parametrization used for the residual part of the  $NN$  interaction. All of these numerical values of the parameters relate to ISM and the density  $n \simeq n_0$ , whereas there is no direct experimental information on their values for  $n > n_0$  and for asymmetric matter. There exist various calculations of the Landau–Migdal parameters as functions of the density for symmetric nuclear matter and for the neutron matter.

To simplify, we may present the spectral function of pions in ISM and for  $\pi^0$  at arbitrary isospin composition as

$$A_\pi(\omega, k) \simeq \sum_i \frac{2\pi \delta(\omega - \omega_i(k))}{\left[2\omega - \frac{\partial \text{Re}\Sigma_\pi^R(\omega, k)}{\partial \omega}\right]_{\omega_i(k)}} + \frac{2\beta_0 k \omega}{\tilde{\omega}^4(k) + \beta_0^2 k^2 \omega^2} \theta(\omega < p_F k / m_N), \quad (23)$$

and the sum is over the quasiparticle-like branches. The second term is due to virtual particle-hole modes. For  $n = n_0$  in ISM, one estimates  $\beta_0 \simeq 0.7$ .

The quantity

$$-G_\pi^{R-1}(\mu_\pi, k) = \tilde{\omega}^2(k) = k^2 + m_\pi^2 - \mu_\pi^2 + \text{Re}\Sigma_\pi(\mu_\pi, k) \quad (24)$$

has the meaning of the squared effective pion gap with a typical behaviour as shown in Figure 9. At  $n > n_c^{(1)}$  (in ISM  $n_c^{(1)} \simeq 0.5\text{--}0.8 n_0$ ), the quantity  $\tilde{\omega}^2$  develops a roton-like minimum  $\tilde{\omega}^2(k) \simeq \tilde{\omega}^2(k_0) + \gamma_0(k^2 - k_0^2)^2 / 4k_0^2$  with some density dependent parameters  $\gamma_0 \sim 1$ ,  $k_0 \simeq p_F$  and the effective pion gap  $\tilde{\omega}(k_0) \equiv \tilde{\omega}$  proves to be  $< m_\pi$ . The effective pion gap determines the degree of the pion-mode softening. The matter for  $n > n_c^{(1)}$  can be treated as a liquid phase of a quantum pion condensate [35,44,48]. At normal nuclear density in ISM, one estimates  $\tilde{\omega}^2(n_0) \simeq 0.8$ . For  $n < n_c^{(1)}$ , there is no minimum at a finite momentum  $k$  and there is no pion softening effect thereby. In the BEM, the pion chemical potentials ( $\mu_{\pi^+} \neq \mu_{\pi^-} \neq 0$ ,  $\mu_{\pi^0} = 0$ ) are determined from equilibrium conditions for the reactions involving pions. In the neutron star matter,  $\mu_{\pi^-}$  follows from the condition of the chemical quasi-equilibrium with respect to the reactions  $n \rightarrow p\pi^-$  and  $n \rightarrow pe\bar{\nu}$ :  $\mu_{\pi^-} = \mu_e = \epsilon_{Fn} - \epsilon_{Fp}$ , where  $\epsilon_{Fn}$ ,  $\epsilon_{Fp}$  are the Fermi energies of the neutron and proton. For small-size systems like atomic nucleus, one should put  $\mu_{\pi^+} = \mu_{\pi^-} = \mu_{\pi^0} = 0$ .

The spectrum of pion quasiparticles possesses three branches for  $\pi^{\pm,0}$  in the ISM and for  $\pi^0$  in asymmetric matter ( $N \neq Z$ ). The spectrum computed for  $n = n_0$  in ISM is shown in Figure 8. In the region  $\omega \gtrsim m_\pi$ , there are two branches: the  $\Delta$  branch and the pion branch. For  $\omega < m_\pi$ , there is the spin-sound branch (with  $\omega \rightarrow 0$  when  $k \rightarrow 0$ ). The hatches show the regions on the  $(\omega, k)$  plane with a non-vanishing pion width, calculated within the quasiparticle approximation for nucleons and  $\Delta$  isobars. The pion spectral function calculated beyond the quasiparticle approximation for nucleons and  $\Delta$ s is more involved even for  $\omega \gtrsim m_\pi$ . In the lower hatched region, at  $\omega < kp_F$  and  $k \sim p_F$ , there are no quasiparticle branches at all and the pion width cannot be neglected. This is the region of the Landau damping in the nucleon particle-hole channel. The pion spectral function is enhanced in this region of  $\omega$  and  $k$  for  $n > n_c^{(1)} \sim (0.5\text{--}0.8) n_0$ . The lowest-energy state determining by the pole of the pion Green function is  $i\beta_0\omega \simeq \tilde{\omega}^2(k_0)$  with  $\beta_0 > 0$  appeared due to the Landau damping. Thus, for  $\tilde{\omega}^2(k_0) > 0$ , the pion excitations die out with time exponentially  $\propto \exp(-\tilde{\omega}^2(k_0)t/\beta_0)$ . With an increase of  $n$ , the quantity  $\tilde{\omega}^2(k_0)$  decreases and may become negative for  $n > n_{c,\pi}$ .

The spectrum of  $\pi^+$  and  $\pi^-$  in isospin asymmetric matter is also reconstructed. For purely neutron matter, it can be found in [25,43].

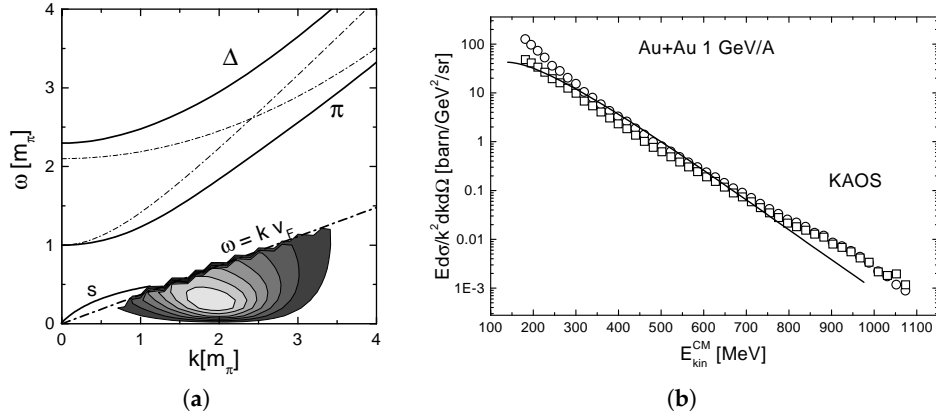


**Figure 8.** Figure from [49]. (a) pion spectrum in ISM at the nuclear saturation density. Dash-dotted lines are the vacuum spectra of pions and  $\Delta$ . Solid lines show quasiparticle branches of pion excitations in medium provided one neglects effects of the particle widths. The contour plot depicts the spectral density of virtual pions; (b) invariant differential cross section of pion production in Au+Au collisions with energy 1 GeV per nucleon as a function of the pion kinetic energy in the center-of-mass system in comparison with experimental data [50] (squares stand for  $\pi^+$  mesons and circles for  $\pi^-$ ).

For  $\tilde{\omega}^2(k_0) < 0$ , the classical pion field begins to grow exponentially during a passage of a time as  $\exp(|\tilde{\omega}^2(k_0)|t/\beta_0)$ . Thus, the change in the sign of  $\tilde{\omega}^2$  at  $n = n_c^\pi$  marks the critical point of a phase transition to a liquid-crystal-like state or solid-like state (depending on the parameters of the matter under consideration, pion species and other conditions) with a classical pion field (a pion condensate). The value of the critical density  $n_c^\pi$  depends on the values of the Landau–Migdal parameters, which are badly known especially for asymmetric matter and for densities significantly larger than  $n_0$ . Nevertheless, some estimations can be given. Various experiments have shown that the pion condensation does not manifest itself in atomic nuclei as a volume effect, see Ref. [25]. Different, although model-dependent, estimations indicate that  $n_c^\pi \sim (1.5\text{--}3) n_0$ , depending on the pion species, the proton-to-neutron ratio and the model used. For example, variational calculations [51] yield  $n_c^\pi \simeq 2 n_0$  for ISM and  $n_c^\pi \simeq 1.3 n_0$  for  $\pi^0$  mesons in the neutron matter.

Assuming that strong interactions manage to keep nuclear system in local quasi-equilibrium up to its breakup and considering the fireball break up as prompt, for the pion distribution of the given species at infinity one gets [25,42,52,53]

$$\frac{dN^\pi}{d^3r d^3k} = 2\sqrt{m_\pi^2 + k^2} \int_0^\infty \frac{d\omega}{(2\pi)^4} \frac{A(\omega, k, T(t_0, \vec{r}), n(t_0, \vec{r}))}{e^{\omega/T(t_0, \vec{r})} - 1}. \quad (25)$$

This expression relates the resulting particle yield to the in-medium spectral density,  $A$ , of excitations, calculated at a freeze out density  $n(t_0, \vec{r})$  and the temperature  $T(t_0, \vec{r})$ . It is assumed that the state has no time to be changed, provided a typical time scale characterizing the fireball expansion  $\tau_{\text{exp}}(n(t_0, \vec{r})) \sim (u/\dot{u})|_{t_0} < 1/|\omega - \sqrt{m_\pi^2 + k^2}|$ . This condition is definitely fulfilled for the pion branch and partially for the  $\Delta$  branch for  $k \gtrsim 1.5 m_\pi$ , but not for virtual particle-hole modes with pion quantum numbers, which can be treated in an opposite, adiabatic approximation. Thus, one can drop contribution of the second term in Equation (23) related to particle-hole excitations with the pion quantum numbers, which have time to die out at the break up stage. Note that the pion momentum is conserved in this sudden freeze out model, but the pion energy is not conserved. The energy of the purely pion sub-system is not conserved. The conservation of the total energy is recovered with taking into account of the energy of the nucleon sub-system.

Exploiting this model for the Au+Au collision at energy  $\sim 1$  GeV per nucleon using the in-medium pion spectrum at freeze-out parameters  $n_b, T_b$  from [42], we obtain the pion yield displayed on the right panel in Figure 8, cf. [49]. A good overall agreement with experimental data for pion momenta 300 MeV

$< k < 700$  MeV is found. Note that the smaller the collision energy, the more pronounced should be the effect of the pion–nucleon interaction on the pion differential cross section. On the contrary, with the increase of the collision energy, the pion softening effects become less pronounced. However, for the baryon-less matter and for  $T \gtrsim m_\pi$  as occurs at RHIC and LHC energies, the in-medium polarization effects become pronounced again [54,55].

Typical density behavior of  $\tilde{\omega}^2(k_0)$  (for  $\pi^\pm, \pi^0$  in ISM and for  $\pi^0$  at  $N \gg Z$ ) is demonstrated in Figure 9.

For  $n < n_c^{(1)}$ ,  $\tilde{\omega}^2(k)$  has a minimum for  $k = k_0 = 0$ , i.e.,  $\tilde{\omega}^2(k_0 = 0) = m_\pi^2$ . Thereby, one may expect a stiffening of the  $NN$  interaction for  $n < n_c^{(1)}$  and, oppositely, the softening for  $n > n_c^{(1)}$ . At the critical point of the pion condensation,  $n = n_c^\pi$ , the value  $\tilde{\omega}^2(k_0)$ , at artificially neglected  $\pi\pi$  fluctuations, changes the sign (see the dashed line in Figure 9).<sup>1</sup> Without taking into account pion fluctuation effects, the pion condensate appears via a second-order phase transition. In reality, the  $\pi\pi$  fluctuations are significant in the vicinity of the critical point and the phase transition is of the first order [44,48,56]. Therefore, we depict branches in Figure 9 (solid curves) with positive and negative values of  $\tilde{\omega}^2(k_0)$ . Calculations in Ref. [48] performed in the Thomas–Fermi approximation demonstrated that, at  $n > n_c^\pi$ , the free energy of the state with  $\tilde{\omega}^2(k_0) > 0$  and without the pion mean field becomes larger than the free energy of the state with  $\tilde{\omega}^2(k_0) < 0$  and a finite pion mean field. Therefore, at  $n > n_c^\pi$ , the state with  $\tilde{\omega}^2(k_0) > 0$  is metastable and the state with  $\tilde{\omega}^2(k_0) < 0$  and the pion mean field  $\varphi_\pi \neq 0$  becomes the ground state. Note that, although qualitative behaviours of the effective pion gap for  $\pi^-$  and  $\pi^0$  mesons in BEM are similar, quantitatively the corresponding values  $\tilde{\omega}$  are different. Only simplifying, one may exploit the very same dependence shown in Figure 9.

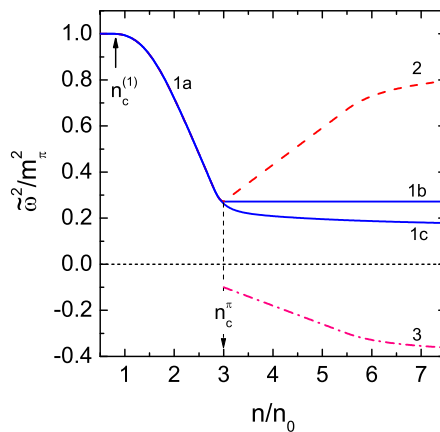


**Figure 9.** Typical density dependence of the effective pion gap squared. The line 1a shows  $\tilde{\omega}^2(k_0, n)$  for  $n_c^{(1)} < n < n_c^\pi$ . For  $n > n_c^\pi$ , the stable state is shown by the line 3. Line 2 demonstrates the quantity  $\tilde{\omega}^2(k_0, n)$  that characterizes a softening of the pion spectrum in the presence of the pion condensate. Line 1c shows a metastable phase in the system where the ground state contains the pion condensate and line 1b demonstrates a possible saturation of the pion softening effect that could be, if the Landau–Migdal parameter  $g'$ , or  $g$ , may increase with an increase of the density.

The quantity  $\tilde{\omega}^2(k_0)$  demonstrates how much the virtual (particle-hole) mode with pion quantum numbers is softened at the given density. Typical momentum transferred in two-nucleon reaction is  $k \simeq p_F$ . For the symmetric nuclear matter at  $n = n_0$ , the ratio  $\alpha = G_\pi^{0,-1}(0, p_F)/G_\pi^{-1}(0, p_F) \simeq 6$ , where  $-G_\pi^{0,-1}(0, p_F) \simeq m_\pi^2 + p_F^2$ , and  $-G_\pi^{-1}(0, p_F) = \tilde{\omega}^2(p_F)$ . We note that this pion softening [25,43] does not significantly enhance the  $NN$  scattering cross section for  $n = n_0$  because of the simultaneous

<sup>1</sup> In order to avoid misunderstanding, by the pion condensation we understand the liquid-crystal-like or solid-like phases (of an inhomogeneous  $k_0 \neq 0$  condensate) rather than a liquid phase mentioned above.



essential suppression of the  $\pi NN$  vertex by nucleon–nucleon correlations. Indeed, the ratio of the  $NN$  cross sections calculated with the free one-pion exchange (FOPE) and medium one-pion exchange (MOPE) models for  $NN$  interaction equals

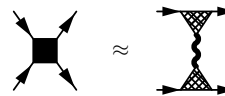
$$R = \frac{\sigma[\text{FOPE}]}{\sigma[\text{MOPE}]} \simeq \frac{\Gamma^4(\omega \simeq 0, k \simeq p_F)(m_\pi^2 + p_F^2)^2}{\tilde{\omega}^4(p_F)}, \tag{26}$$

where  $\Gamma$  is the vertex dressing factor determined by Equations (18) and (22), and  $\Gamma(n_0) \simeq 0.4$ . For  $n \lesssim n_0$ , one has  $R \lesssim 1$ , whereas already for  $n = 2 n_0$  this estimate yields  $R \sim 10$ . Thus, following Equation (26), one can evaluate the  $NN$  interaction for  $n > n_0$  with the help of the MOPE, i.e., one approximately has



$$\tag{27}$$

Here, the bold wavy line relates to the in-medium pion. In the soft-pion approximation, the same one-pion exchange determines also interaction in the particle–particle channel



$$\tag{28}$$

For example, this quantity determines the  $NN$  interaction entering neutrino emissivities of the two-nucleon processes (see the next section).

Kaons as pions are also modified in nuclear matter. Here, the most important are hyperon–nucleon-hole diagrams [57,58] and the  $s$ -wave scattering kaon–nucleon interaction being stronger in the kaon case. On the left panel of Figure 10 a spectral density of  $K^-$  excitations in ISM at saturation is shown. On the right panel, results are presented of calculations of the invariant differential cross section of  $K^-$  production in Ni+Ni collisions with energy 1.8 GeV per nucleon as the function of the kaon kinetic energy in the center-of-mass system [59] in comparison with the experimental data [60,61]. For these calculations, one used the spectral function of  $K^-$  shown on the left panel and the prompt freeze-out model (see Equation (25) above). As above, the fireball dynamics were considered within the expanding fireball model [42]. We see a good overall agreement of calculations taking into account of in-medium polarization effects with the data.

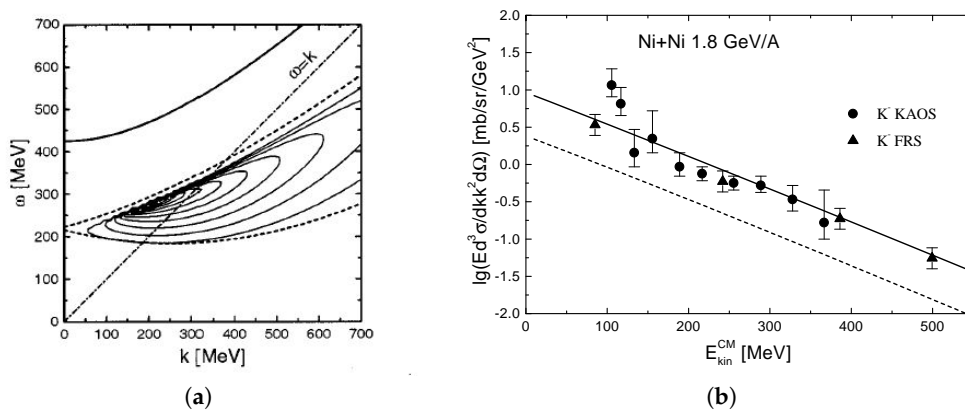


**Figure 10.** Figure from [49]. (a) spectral density of  $K^-$  excitations in ISM at saturation. The upper curve shows the position of the quasiparticle kaon branch. Dashed curves border the  $(\Lambda p^{-1})$  continuum. Thin lines between them depict the ascending levels of kaon spectral density; (b) invariant differential cross section of  $K^-$  production in Ni+Ni collisions with energy 1.8 GeV per nucleon as the function of the kaon kinetic energy in the center-of-mass system in comparison with experimental data [60,61]. The solid line depicts calculations with the in-medium spectral density, and the dashed line shows the results for the free kaon spectrum.

### 5. Pion Softening and Neutrino Emission from Neutron Stars

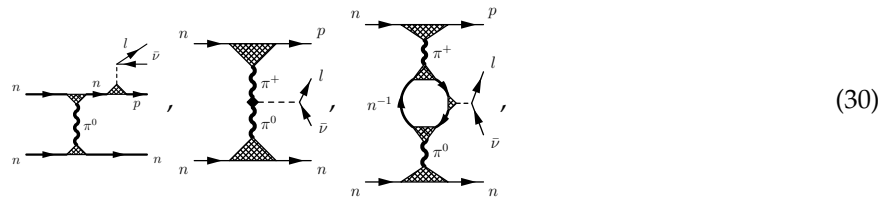
After first tens of seconds (at most hours), the typical temperature of a neutron star decreases below the neutrino-opacity temperature  $T_{\text{opac}} \sim \text{MeV}$ . For  $T < T_{\text{opac}}$ , the neutrino mean-free path becomes longer than the star radius and neutrinos are radiated directly from the star interior without subsequent rescattering [62–66]. Hence, the star can be considered for neutrinos as a warm “white” body. In this sense, the problem is somewhat similar to the problem of the di-lepton radiation from the nuclear fireball prepared in heavy-ion collisions. Typically averaged lepton energy ( $\sim$ several  $T$ ) is much larger than the nucleon particle width  $\Gamma_N \sim T^2/\epsilon_F$ . Therefore, nucleons can be treated within the quasiparticle approximation. Then, the processes can be separated according to their phase space: the direct Urca (DU) one-nucleon processes,  $n \rightarrow pe\bar{\nu}$  (if they are not forbidden by the energy-momentum conservation) have the largest emissivity,  $\epsilon_\nu \propto T^6$  for non-superfluid systems, the modified Urca (MU) two-nucleon processes  $nn \rightarrow npe\bar{\nu}$ ,  $np \rightarrow ppe\bar{\nu}$  and nucleon bremsstrahlung (NB) processes  $nn \rightarrow nn\nu\bar{\nu}$ ,  $np \rightarrow np\nu\bar{\nu}$ , have a lesser emissivity,  $\epsilon_\nu \propto T^8$ , and so on. The DU emissivity proves to be so high that if DU reactions occurred in a majority of neutron stars, they could not be visible in soft X-rays in disagreement with observations. The requirement of the absence of the DU processes in neutron stars with  $M < 1.5 M_\odot$  puts a constraint [1,8,67] on the density dependence of the symmetry energy, which is also an important quantity for the description of heavy-ion reactions. Within EoSs that we use (KVORcut-based and MKVOR-based), the one-nucleon DU processes are forbidden by energy-momentum conservation at least for light ( $M \sim 1 M_\odot$ ) and medium-heavy  $\lesssim 1.5 M_\odot$  neutron stars and the most efficient reactions become processes involving two nucleons.

In the so-called *standard scenario* of the neutron star cooling [68,69], the processes were calculated without taking into account in-medium effects. The MU processes were considered as the most important channel for temperatures up to  $T \sim 10^8\text{--}10^9$  K. Then, based on the standard scenario, the so-called *minimal cooling paradigm* was proposed [70], where medium effects were assumed to play only a minor role. For evaluation of the MU and the NB neutrino emissivity within this paradigm, one uses the FOPE model of Friman and Maxwell [71]. The density dependence of the reaction rates calculated with the FOPE model is very weak and thereby the neutrino radiation from a neutron star depends very weakly on the star mass. It proves to be that the existing data on the time dependence of the surface temperatures of pulsars are then hardly explained. The agreement can be achieved only with inclusion of the efficient DU reaction in a majority of neutron stars and at the price that neutron stars measured in soft X-rays should then have approximately the same masses. The latter assumption disagrees with a broad distribution of neutron stars over the masses, as follows from the population synthesis modeling. Based on the assumption that the mass distribution of those objects for which surface temperatures are measured is similar to the one extracted, e.g., from a population synthesis analysis and from supernova simulations, the very efficient DU reaction should be forbidden in the majority of the former neutron stars. We add here that measurements of the high masses of the pulsars PSR J1614-2230 [72,73] and PSR J0348-0432 [4] and of the low masses for PSR J0737-3039B [74] for the companion of PSR J1756-2251 [75,76] and the companion of PSR J0453+1559 have provided the proof for the existence of neutron stars with masses varying at least from 1.2 to  $1.97 M_\odot$ .

Refs. [25,62–66] calculated the rate of the two-nucleon processes taking into account in-medium effects. As we have argued, for  $n \gtrsim n_0$ , the  $NN$  interaction amplitude might be mainly controlled by the soft pion exchange. Thus, instead of the FOPE-based MU diagram



(zig-zag line corresponds to the free pion, dot, to the free vertices), one has as a generalization a medium one-pion exchange (MOPE) for the medium-modified Urca (MMU) processes:



where the bold-wavy line corresponds to the dressed pion and the hatched vertex takes into account the  $NN$  correlations. The first diagram naturally generalizes the corresponding MU (FOPE) contribution (29). Evaluations have shown that it gives a smaller contribution in the emissivity for  $n \gtrsim n_0$  than what comes from the processes occurring through intermediate reaction states, as shown by the second and third diagrams (30). Note that these diagrams are absent, if one approximates the nucleon–nucleon interaction by a two-body potential.

At  $T < T_c \lesssim (0.1-1)$ , MeV nucleons form Cooper pairs. The emissivities of the processes with participation of nucleons are then suppressed by the corresponding phase-space suppression factors. However, a new nucleon pair-breaking-formation (PBF) reaction channel  $N \rightarrow N\nu\bar{\nu}$  is opened up for  $T < T_c$ , cf. [64,65,77]. This process was also included in calculations of the neutrino emissivity within the minimal cooling paradigm [70,78].

On the other hand, the *nuclear medium cooling scenario* was developed, where besides the MMU processes and the medium-modified nucleon bremsstrahlung (MNB) processes [63], the PBF processes [64,65,79–81] and other ones were incorporated. The results of calculations were confronted to the data [67,82–86] demonstrating an overall agreement of calculations with the data already without necessity to include the DU channel. An example of such calculations is presented in Figure 11, where the cooling curves are shown being computed with MKVOR EoS [87]. The effective pion gap was used following the solid curve 1a + 1b in Figure 9. The pairing  $1S_0$  gaps correspond to calculations with the EEHO model, cf. similar results of calculations with DD2 EoS in Figure 3 of [86].

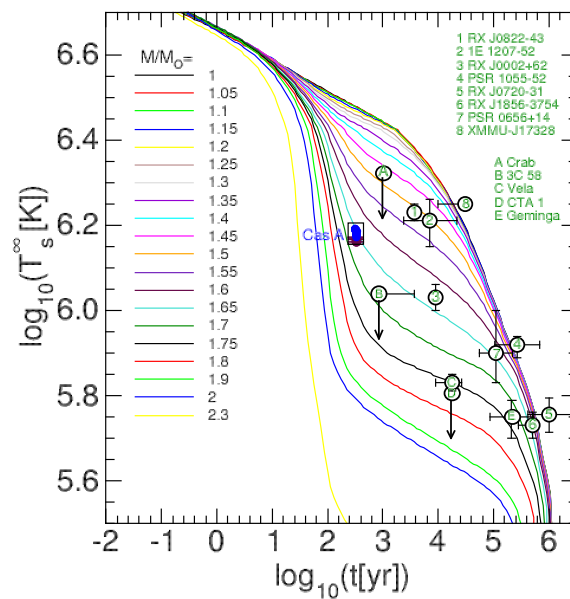


**Figure 11.** Figure from H. Grigorian calculations with MKVOR EoS [87].  $T_s^\infty$  is the redshifted surface temperature,  $t$  is the neutron star age. The effective pion gap is given by the solid curve 1a + 1b in Figure 9. The pairing  $1S_0$  gaps correspond to calculations with the EEHO model. The mass range is shown in the legend.

## 6. Viscosity of Neutron-Star Matter and $r$ -Modes in Rotating Pulsars

Neutron stars are typically formed rapidly rotating with a Kepler rotation frequency  $\nu_{in} \sim 1$  kHz. However, the majority of young ( $\lesssim 10^5$  y age) pulsars have rotation frequencies less than 10 Hz, and the fastest young pulsar PSR J0537-6910 (of age  $\sim 5000$  y) rotates with the frequency  $\nu = \nu_{max}^{young} = 62$  Hz. An efficient mechanism allowing to decelerate rotation of a neutron star already at an early stage of its evolution is the  $r$ -mode instability [88,89]. The  $r$ -mode oscillations, related to Rossby waves in Earth atmosphere and oceans, lead to emission of gravitational waves, which carry away most of the initial angular momentum of a star and the star rotation decelerates. The  $r$ -modes would grow exponentially for any rotation frequency, if not a damping because of a viscosity of a warm neutron star matter [90]. The typical temperature in the interior of a pulsar of age  $\sim 5000$  y is  $\sim 2 \times 10^7 - 5 \times 10^8$  K, depending on the mass of the star and the cooling scenario, whereas the  $r$ -mode instability proves to be the strongest at higher temperatures  $T \sim 10^9$  K. Hence, young pulsars have passed through an instability phase during their early history and thus one should demonstrate that, after the instability phase, the pulsar frequencies remain larger than  $\nu_{max}^{young}$ . Different mechanisms for suppression of the instability were studied. Most attempts were spent to find appropriate arguments to increase the values of shear and bulk viscosities, increasing thereby damping of modes. However, it was concluded, e.g., see [91], that the minimum value of the frequency at the  $r$ -mode stability boundary  $\nu_c(T)$  proves to be less than  $\nu_{max}^{young}$ , if one uses standard dissipation mechanisms only not including the DU reactions.

Refs. [92,93] studied how the viscosity of the neutron-star matter influences the  $r$ -mode instability in rotating neutron stars provided a pion softening effect is included. For  $n > n_c^\pi$ , two possibilities were studied: one corresponding to saturation of the pion softening (see lines 1b and 1c in Figure 9) and the other including pion condensation (lines 3 and 2). In the latter case, the pion Urca (PU) processes, like  $p\pi_c^- \rightarrow pe\bar{\nu}$ ,  $n\pi_c^0 \rightarrow pe\bar{\nu}$ , were included. The neutron–neutron and proton–proton Cooper pairing effects were also incorporated. In the shear viscosity, the lepton contribution was calculated with taking into account of the Landau damping in the photon exchange as was done in [94], the nucleon contribution described by the MOPE, and some other terms, such as the phonon contribution in the  $1S_0$  superfluid neutron phase, and the neutrino term in the neutrino opacity region of temperatures. It proves to be that the term in the bulk viscosity from the two-nucleon MMU reactions possesses the strongest density dependence (rising by several orders of magnitude for massive stars) because of the pion softening. In addition, contributions to the bulk viscosity arising from other reactions induced by charged weak currents, e.g., in the PU processes and DU processes, were included. The radiative bulk viscosity induced by charged and neutral weak currents in the region of the neutrino transparency of the star was also calculated while taking into account in-medium effects.

The characteristic time scale of the evolution of the  $r$ -mode amplitude is given by

$$\tau^{-1} = -\tau_G^{-1} + \tau_\eta^{-1} + \tau_\zeta^{-1}, \quad (31)$$

where  $\tau_G$  is the typical time of the gravitational radiation,  $\tau_\eta$  is the relaxation time due to the shear viscosity, and  $\tau_\zeta$  is the relaxation time due to the bulk viscosity. The  $r$ -modes become stable, provided  $\tau^{-1} > 0$ .

We exploited the EoS similar to the Akmal–Pandharipande–Ravenhall EoS up to  $4n_0$ , but stiffer at higher densities, producing the maximum neutron star mass compatible with observations. Within this EoS, the DU processes do not appear up to  $5n_0$  (corresponding to the star mass  $M \simeq 1.9 M_\odot$ ). To compute MMU processes, we use curves 1a + 1b in Figure 9 and, for MMU + PU, ones we exploit curves 1a + 2 for MMU and 3 for PU.

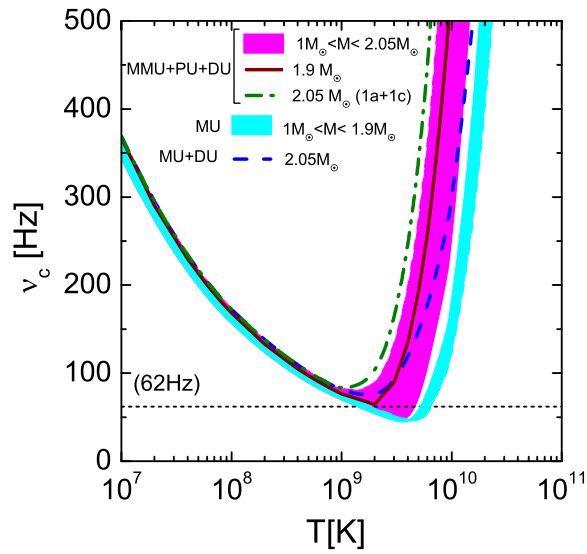


**Figure 12.** Figure from [93]. Critical frequency of the  $r$ -mode instability as a function of the temperature for a band of neutron star masses. Dashed line shows calculation with MU + DU for  $M = 2.05 M_{\odot}$ . The solid line demonstrates calculation done for the threshold mass of the DU processes within MMU + PU + DU scenario. The dashed-dotted line shows calculation with MMU computed with 1a + 1c curve in Figure 9 for  $M = 2.05 M_{\odot}$ .

Equation  $\tau^{-1} = 0$  was solved with all contributions to the shear and bulk viscosities taken into account. The solutions are presented in Figure 12 as functions of the temperature for neutron star masses from  $M_{\odot} < M < 2.05 M_{\odot}$ . Within the minimal cooling scenario, when in-medium effects are not included,  $\nu_{c,\min}$  exceeds  $\nu_{\max}^{\text{young}}$  only for the masses  $M > 2.03 M_{\odot}$  (when DU reaction is already efficient), i.e., very close to the maximum mass,  $2.05 M_{\odot}$ . However, if initially the star passes through the instability region, the developed  $r$ -modes may blow off some part of the star matter. Thus, its final mass can hardly be very close to the maximum mass. Alternatively, the experimental value of the pulsar PSR J0537-6910 could be explained within the minimal cooling scenario, if one exploited the EoS that allows for a lower DU threshold density. Within the nuclear medium cooling scenario, the DU processes are not needed to explain the stability of PSR J0537-6910. We may explain it for  $M > 1.804 M_{\odot}$ , if calculations of MMU processes are done using curves 1a + 2, and 3 for PU, and for  $M > 1.776$  provided we use curves 1a + 1c to calculate MMU, without PU. For the MMU case (for curves 1a + 1b for MMU without PU), PSR J0537-6910 mass should be  $M > 1.84 M_{\odot}$ . In the figure legend symbol, MMU + DU means that MMU and DU (for  $n > n_c^{\text{DU}}$ ) reactions are included and MMU + PU + DU means that PU processes (for  $n > n_c^{\text{PU}}$ ) are included as well.

## 7. Conclusions

In the given contribution, I considered some specific but common problems in neutron-star and heavy-ion-collision physics, where in-medium effects play an important role. First, I discussed an effect of a scaling of the effective hadron masses and couplings on the equation of state of the baryon matter. Then, an important role was clarified, played by the shear and bulk viscosities and the thermal conductivity as driving forces of the first-order phase transitions. Next, the baryon-medium polarization effects on the pion and kaon propagation in dense matter were reviewed. Special attention was attended to the pion softening effect, and its particular role was indicated in the problem of neutrino radiation from neutron stars. Finally, viscosity effects, by taking into account the pion softening on the stability of  $r$ -modes in young pulsars, were analysed.

**Acknowledgments:** I thank David Blaschke, Hovik Grigorian, Evgeni E. Kolomeitsev and Konstantin A. Maslov for the help and advice. The research was supported by the Ministry of Education and Science of the Russian Federation within the state assignment, project No. 3.6062.2017/BY, by the Russian Foundation for Basic Research (RFBR) according to the research project No. 16-02-00023-A (Sections 2.3, 2.4 and 4), and by the Russian Science Foundation, Grant No. 17-12-01427 (Section 3.2).

**Conflicts of Interest:** The author declares no conflict of interest.

## Abbreviations

All necessary abbreviations are introduced in the paper body. For convenience some of them are repeated below:

EoS	Equation of state
BEM	Beta-equilibrium matter
ISM	Isospin-symmetric matter
RMF model	Relativistic mean-field model
NLW model	Nonlinear Walecka model
DU process	Direct Urca process
MU	modified Urca
MMU	medium modified Urca
PU	pion (condensate) Urca
NB	nucleon bremsstrahlung
MNB	medium-modified nucleon bremsstrahlung
PBF	Pair-breaking-formation
FOPE	Free one-pion exchange
MOPE	Medium one-pion exchange

## References

1. Klähn, T.; Blaschke, D.; Typel, S.; Van Dalen, E.N.; Faessler, A.; Fuchs, C.; Gaitanos, T.; Grigorian, H.; Ho, A.; Kolomeitsev, E.E.; et al. Constraints on the high-density nuclear equation of state from the phenomenology of compact stars and heavy-ion collisions. *Phys. Rev. C* **2006**, *74*, 035802.
2. Danielewicz, P.; Lacey, R.; Lynch, W.G. Determination of the equation of state of dense matter. *Science* **2002**, *298*, 1592–1596.
3. Lynch, W.G.; Tsang, M.B.; Zhang, Y.; Danielewicz, P.; Famiano, M.; Li, Z.; Steiner, A.W. Probing the Symmetry Energy with Heavy Ions. *Prog. Part. Nucl. Phys.* **2009**, *62*, 427–432.
4. Antoniadis, J.; Freire, P.C.; Wex, N.; Tauris, T.M.; Lynch, R.S.; van Kerkwijk, M.H.; Kramer, M.; Bassa, C.; Dhillon, V.S.; Driebe, T.; et al. A Massive Pulsar in a Compact Relativistic Binary. *Science* **2013**, *340*, 1233232.
5. Abbott, B.P.; Abbott, R.; Abbott, T.D.; Acernese, F.; Ackley, K.; Adams, C.; Adams, T.; Addesso, P.; Adhikari, R.X.; Adya, V.B.; et al. GW170817: Observation of Gravitational Waves from a Binary Neutron Star Inspiral. *Phys. Rev. Lett.* **2017**, *119*, 161101.
6. Khvorostukhin, A.S.; Toneev, V.D.; Voskresensky, D.N. Equation of State for Hot and Dense Matter:  $\sigma$ - $\omega$ - $\rho$  Model with Scaled Hadron Masses and Couplings. *Nucl. Phys. A* **2007**, *791*, 180–221.
7. Khvorostukhin, A.S.; Toneev, V.D.; Voskresensky, D.N. Relativistic Mean-Field Model with Scaled Hadron Masses and Couplings. *Nucl. Phys. A* **2008**, *813*, 313–346.
8. Kolomeitsev, E.E.; Voskresensky, D.N. Relativistic mean-field models with effective hadron masses and coupling constants, and rho- condensation. *Nucl. Phys. A* **2005**, *759*, 373–413.
9. Maslov, K.A.; Kolomeitsev, E.E.; Voskresensky, D.N. Solution of the Hyperon Puzzle within a Relativistic Mean-Field Model. *Phys. Lett. B* **2015**, *748*, 369–375.
10. Maslov, K.A.; Kolomeitsev, E.E.; Voskresensky, D.N. Relativistic Mean-Field Models with Scaled Hadron Masses and Couplings: Hyperons and Maximum Neutron Star Mass. *Nucl. Phys. A* **2016**, *950*, 64–109.
11. Kolomeitsev, E.E.; Maslov, K.A.; Voskresensky, D.N. Delta isobars in relativistic mean-field models with  $\sigma$ -scaled hadron masses and couplings. *Nucl. Phys. A* **2016**, *961*, 106–141.
12. Maslov, K.A.; Kolomeitsev, E.E.; Voskresensky, D.N. Making a soft relativistic mean-field equation of state stiffer at high density. *Phys. Rev. C* **2016**, *92*, 052801.
13. Voskresensky, D.N. Comments on manifestation of in-medium effects in heavy-ion collisions. *Eur. Phys. J. A* **2016**, *52*, 223.

14. Kolomeitsev, E.E.; Maslov, K.A.; Voskresensky, D.N. Charged  $\rho$ -meson condensation in neutron stars. *Nucl. Phys. A* **2018**, *970*, 291–315.
15. Schaffner-Bielich, J. Hypernuclear Physics for Neutron Stars. *Nucl. Phys. A* **2008**, *804*, 309–321.
16. Djapo, H.; Schaefer, B.J.; Wambach, J. On the appearance of hyperons in neutron stars. *Phys. Rev. C* **2010**, *81*, 035803.
17. Drago, A.; Lavagno, A.; Pagliara, G.; Pigato, D. Early appearance of  $\Delta$  isobars in neutron stars. *Phys. Rev. C* **2014**, *90*, 065809.
18. Drago, A.; Lavagno, A.; Pagliara, G.; Pigato, D. The scenario of two families of compact stars: Part 1. Equations of state, mass–radius relations and binary systems. *Eur. Phys. J. A* **2016**, *52*, 41.
19. Riek, F.; Lutz, M.F.M.; Korpa, C.L. Photoabsorption off nuclei with self consistent vertex corrections. *Phys. Rev. C* **2008**, *80*, 024902.
20. Voskresensky, D.N. On the possibility of the condensation of the charged rho meson field in dense isospin asymmetric baryon matter. *Phys. Lett. B* **1997**, *392*, 262–266.
21. Chernodub, M.N. Electromagnetic superconductivity of vacuum induced by strong magnetic field. *Lect. Notes Phys.* **2013**, *871*, 143–180.
22. Mallick, R.; Schramm, S.; Dexheimer, V.; Bhattacharyya, A. On the possibility of rho-meson condensation in neutron stars. *Mon. Not. R. Astron. Soc.* **2015**, *449*, 1347–1351.
23. Voskresensky, D.N.; Senatorov, A.V.; Kampf, B.; Haubold, H.J. A possible explanation of the second neutrino burst in SN1987A. *Astrophys. Space Sci.* **1987**, *138*, 421–424.
24. Haubold, H.J.; Kampf, B.; Senatorov, A.V.; Voskresensky, D.N. A Tentative approach to the second neutrino burst in SN1987A. *Astron. Astrophys.* **1988**, *191*, L22–L24.
25. Migdal, A.B.; Saperstein, E.E.; Troitsky, M.A.; Voskresensky, D.N. Pion degrees of freedom in nuclear matter. *Phys. Rept.* **1990**, *192*, 179–437.
26. Galeotti, P.; Pizzella, G. New analysis for the correlation between gravitational wave and neutrino detectors during SN1987A. *Eur. Phys. J. C* **2016**, *76*, 426.
27. Prakash, M.; Bombaci, I.; Prakash, M.; Ellis, P.J.; Lattimer, J.M.; Knorren, R. Composition and structure of protoneutron stars. *Phys. Rept.* **1997**, *280*, 1–77.
28. Skokov, V.V.; Voskresensky, D.N. Hydrodynamical description of a hadron–quark first-order phase transition. *JETP Lett.* **2009**, *90*, 223–227.
29. Skokov, V.V.; Voskresensky, D.N. Hydrodynamical description of first-order phase transitions: Analytical treatment and numerical modeling. *Nucl. Phys. A* **2009**, *828*, 401–438.
30. Skokov, V.V.; Voskresensky, D.N. Thermal conductivity in dynamics of first-order phase transition. *Nucl. Phys. A* **2010**, *847*, 253–267.
31. Skokov, V.V.; Voskresensky, D.N. Viscosity and thermal conductivity effects at first-order phase transitions in heavy-ion collisions. *Phys. Atom. Nucl.* **2012**, *75*, 770–775.
32. Randrup, J. Phase transition dynamics for baryon-dense matter. *Phys. Rev. C* **2009**, *79*, 054911.
33. Steinheimer, J.; Randrup, J. Spinodal density enhancements in simulations of relativistic nuclear collisions. *Phys. Rev. C* **2013**, *87*, 054903.
34. Romatschke, P.; Romatschke, U. Viscosity Information from Relativistic Nuclear Collisions: How Perfect is the Fluid Observed at RHIC? *Phys. Rev. Lett.* **2007**, *99*, 172301.
35. Voskresensky, D.N. Quasiclassical description of condensed systems by a complex order parameter. *Phys. Scr.* **1993**, *47*, 333–354.
36. Glendenning, N.K. First order phase transitions with more than one conserved charge: Consequences for neutron stars. *Phys. Rev. D* **1992**, *46*, 1274–1287.
37. Heiselberg, H.; Pethick, C.J.; Staubo, E.F. Quark matter droplets in neutron stars. *Phys. Rev. Lett.* **1993**, *70*, 1355–1359.
38. Voskresensky, D.N.; Yasuhira, M.; Tatsumi, T. Charge screening at first order phase transitions. *Phys. Lett. B* **2002**, *541*, 93–100.
39. Voskresensky, D.N.; Yasuhira, M.; Tatsumi, T. Charge screening at first order phase transitions and hadron quark mixed phase. *Nucl. Phys. A* **2003**, *723*, 291–339.
40. Maruyama, T.; Tatsumi, T.; Voskresensky, D.N.; Tanigawa, T.; Endo, T.; Chiba, S. Finite size effects on kaonic pasta structures. *Phys. Rev. C* **2006**, *73*, 035802.

41. Maruyama, T.; Tatsumi, T.; Voskresensky, D.N.; Tanigawa, T.; Chiba, S. Nuclear pasta structures and the charge screening effect. *Phys. Rev. C* **2005**, *72*, 015802.
42. Voskresensky, D.N. Many particle effects in nucleus-nucleus collisions. *Nucl. Phys. A* **1993**, *555*, 293–328.
43. Migdal, A.B. Pion Fields in Nuclear Matter. *Rev. Mod. Phys.* **1978**, *50*, 107–172.
44. Voskresensky, D.N.; Mishustin, I.N. Polarization operator of pions at finite temperatures. *Yad. Fiz.* **1982**, *35*, 1139–1156.
45. Kolomeitsev, E.E.; Voskresensky, D.N. Superfluid nucleon matter in and out of equilibrium and weak interactions. *Phys. Atom. Nucl.* **2011**, *74*, 1316–1363.
46. Roepke, G.; Voskresensky, D.; Kryukov, I.; Blaschke, D. Fermi liquid, clustering, and structure factor in dilute warm nuclear matter. *Nucl. Phys. A* **2018**, *970*, 224–258.
47. Migdal, A.B. *Theory of Finite Fermi Systems and Properties of Atomic Nuclei*; Wiley and Sons, New York, USA, 1967; 2-nd ed.; Nauka: Moscow, Russia, 1983.
48. Dyugaev, A.M. Crystalline And Liquid Phases Of A Pion Condensate. *Pisma Zh. Eksp. Teor. Fiz.* **1982**, *35*, 341–344.
49. Kolomeitsev, E.E.; Voskresensky, D.N. Meson particle hole dynamics. *arXiv* **2000**, arXiv:nucl-th/0001062.
50. Wagner, A.; Muntz, C.; Oeschler, H.; Sturm, C.; Barth, R.; Cieslak, M.; Debowski, M.; Grosse, E.; Koczon, P.; Mang, M.; et al. Evidence for different freezeout radii of high-energy and low-energy pions emitted in Au + Au collisions at 1-A/GeV. *Phys. Lett. B* **1998**, *420*, 20–24.
51. Akmal, A.; Pandharipande, V.R.; Ravenhall, D.G. The Equation of state of nucleon matter and neutron star structure. *Phys. Rev. C* **1998**, *58*, 1804–1828.
52. Senatorov, A.V.; Voskresensky, D.N. Pion Dynamics in Heavy Ion Collisions. *Phys. Lett. B* **1989**, *219*, 31–34.
53. Voskresensky, D.N.; Blaschke, D.; Roepke, G.; Schulz, H. Nonequilibrium approach to dense hadronic matter. *Int. J. Mod. Phys. E* **1995**, *4*, 1–45.
54. Voskresensky, D.N. Hadron liquid with a small baryon chemical potential at finite temperature. *Nucl. Phys. A* **2004**, *744*, 378–444.
55. Voskresensky, D.N. Thermodynamics of resonances and blurred particles. *Nucl. Phys. A* **2008**, *812*, 158–185.
56. Dyugaev, A.M. Nature of Phase Transition in Case of pi- Condensation. *Pisma Zh. Eksp. Teor. Fiz.* **1975**, *22*, 181–185.
57. Kolomeitsev, E.E.; Kampfer, B.; Voskresensky, D.N. Kaon polarization in nuclear matter. *Nucl. Phys. A* **1995**, *588*, 889–917.
58. Kolomeitsev, E.E.; Voskresensky, D.N. Negative kaons in dense baryonic matter. *Phys. Rev. C* **2003**, *68*, 015803.
59. Kolomeitsev, E.E.; Kampfer, B.; Voskresensky, D.N. The impact of kaon polarization in nuclear matter on the K- production in heavy ion collisions. *Int. J. Mod. Phys. E* **1996**, *5*, 313–328.
60. Barth, R.; Senger, P.; Ahner, W.; Beckerle, P.; Bormann, C.; Brill, D.; Cieslak, M.; Grosse, E.; Koczoń, P.; Kohlmeyer, B.; et al. Subthreshold production of kaons and anti-kaons in nucleus-nucleus collisions at equivalent beam energies. *Phys. Rev. Lett.* **1997**, *78*, 4007–4010.
61. Schröter, A.; Berdermann, E.; Geissel, H.; Gillitzer, A.; Homolka, J.; Kienle, P.; Koenig, W.; Povh, B.; Schumacher, F.; Ströher, H. Subthreshold anti-proton and K- production in heavy ion collisions. *Z. Phys. A Hadron. Nucl.* **1994**, *350*, 101–113.
62. Voskresensky, D.N.; Senatorov, A.V. Pion Excitations In A Nucleonic Medium May Be Pertinent To The Luminosity Of Neutron Stars. *Pisma Zh. Eksp. Teor. Fiz.* **1984**, *40*, 395–398.
63. Voskresensky, D.N.; Senatorov, A.V. Emission of Neutrinos by Neutron Stars. *Zh. Eksp. Teor. Fiz.* **1986**, *90*, 1505–1526.
64. Senatorov, A.V.; Voskresensky, D.N. Collective Excitations in Nucleonic Matter and the Problem of Cooling of Neutron Stars. *Phys. Lett. B* **1987**, *184*, 119–124.
65. Voskresensky, D.N.; Senatorov, A.V. Description of Nuclear Interaction in Keldysh's Diagram Technique and Neutrino Luminosity of Neutron Stars. *Yad. Fiz.* **1987**, *45*, 657–669. (In Russian)
66. Voskresensky, D.N. Neutrino cooling of neutron stars: Medium effects. In *Physics of Neutron Star Interiors*; Springer: Berlin/Heidelberg, Germany, 2001; pp. 467–503.
67. Blaschke, D.; Grigorian, H.; Voskresensky, D.N. Cooling of neutron stars: Hadronic model. *Astron. Astrophys.* **2004**, *424*, 979–992.
68. Tsuruta, S. Thermal properties and detectability of neutron stars. I. Cooling and heating of neutron stars. *Phys. Rep.* **1979**, *56*, 237–277.



69. Shapiro, S.; Teukolsky, S.A. *Black Holes, White Dwarfs and Neutron Stars: The Physics of Compact Objects*; Wiley: New York, NY, USA, 1983; Chapter 11.
70. Page, D.; Lattimer, J.M.; Prakash, M.; Steiner, A.W. Minimal cooling of neutron stars: A New paradigm. *Astrophys. J. Suppl. Ser.* **2004**, *155*, 623–650.
71. Friman, B.L.; Maxwell, O.V. Neutron Star Neutrino Emissivities. *Astrophys. J.* **1979**, *232*, 541–557.
72. Demorest, P.; Pennucci, T.; Ransom, S.; Roberts, M.; Hessels, J. Shapiro Delay Measurement of A Two Solar Mass Neutron Star. *Nature* **2010**, *467*, 1081–1083.
73. Fonseca, E.; Pennucci, T.T.; Ellis, J.A.; Stairs, I.H.; Nice, D.J.; Ransom, S.M.; Demorest, P.B.; Arzoumanian, Z.; Crowter, K.; Dolch, T.; et al. The NANOGrav Nine-year Data Set: Mass and Geometric Measurements of Binary Millisecond Pulsars. *Astrophys. J.* **2016**, *832*, 167.
74. Kramer, M.; Stairs, I.H.; Manchester, R.N.; McLaughlin, M.A.; Lyne, A.G.; Ferdman, R.D.; Burgay, M.; Lorimer, D.R.; Possenti, A.; D’Amico, N.; et al. Tests of general relativity from timing the double pulsar. *Science* **2006**, *314*, 97–102.
75. Faulkner, A.J.; Kramer, M.; Lyne, A.G.; Manchester, R.N.; McLaughlin, M.A.; Stairs, I.H.; Hobbs, G.; Possenti, A.; Lorimer, D.R.; D’Amico, N.; et al. PSR J1756-2251: A New relativistic double neutron star system. *Astrophys. J.* **2004**, *618*, L119-L122.
76. Ferdman, R.D.; Stairs, I.H.; Kramer, M.; Janssen, G.H.; Bassa, C.G.; Stappers, B.W.; Demorest, P.B.; Cognard, I.; Desvignes, G.; Theureau, G.; et al. PSR J1756-2251: A pulsar with a low-mass neutron star companion. *Mon. Not. R. Astron. Soc.* **2014**, *443*, 2183–2196.
77. Flowers, E.; Ruderman, M.; Sutherland, P. Neutrino pair emission from finite-temperature neutron superfluid and the cooling of young neutron stars. *Astrophys. J.* **1976**, *205*, 541–544.
78. Yakovlev, D.G.; Kaminker, A.D.; Gnedin, O.Y.; Haensel, P. Neutrino emission from neutron stars. *Phys. Rep.* **2001**, *354*, 1–55.
79. Kolomeitsev, E.E.; Voskresensky, D.N. Neutrino emission due to Cooper-pair recombination in neutron stars revisited. *Phys. Rev. C* **2008**, *77*, 065808.
80. Kolomeitsev, E.E.; Voskresensky, D.N. Neutral weak currents in nucleon superfluid Fermi liquids: Larkin-Migdal and Leggett approaches. *Phys. Rev. C* **2010**, *81*, 065801.
81. Kolomeitsev, E.E.; Voskresensky, D.N. Spin excitonic and diffusive modes in superfluid Fermi liquids. *Phys. Rev. C* **2011**, *84*, 068801.
82. Schaab, C.; Voskresensky, D.; Sedrakian, A.D.; Weber, F.; Weigel, M.K. Impact of medium effects on the cooling of nonsuperfluid and superfluid neutron stars. *Astron. Astrophys.* **1997**, *321*, 591–604.
83. Grigorian, H.; Voskresensky, D.N. Medium effects in cooling of neutron stars and 3P(2) neutron gap. *Astron. Astrophys.* **2005**, *444*, 913–929.
84. Blaschke, D.; Grigorian, H.; Voskresensky, D.N.; Weber, F. On the Cooling of the Neutron Star in Cassiopeia A. *Phys. Rev. C* **2012**, *85*, 022802.
85. Blaschke, D.; Grigorian, H.; Voskresensky, D.N. Nuclear medium cooling scenario in the light of new Cas A cooling data and the  $2M_{\odot}$  pulsar mass measurements. *Phys. Rev. C* **2013**, *88*, 065805.
86. Grigorian, H.; Voskresensky, D.N.; Blaschke, D. Influence of the stiffness of the equation of state and in-medium effects on the cooling of compact stars. *Eur. Phys. J. A* **2016**, *52*, 1–19.
87. Grigorian, H.; Kolomeitsev, E.E.; Maslov, K.A.; Voskresensky, D.N. On cooling of neutron stars with stiff equation of state including hyperons. *arXiv* **2017**, arXiv:1801.00040.
88. Andersson, N. A New class of unstable modes of rotating relativistic stars. *Astrophys. J.* **1998**, *502*, 708–713.
89. Friedman, J.L.; Morsink, S.M. Axial instability of rotating relativistic stars. *Astrophys. J.* **1998**, *502*, 714–720.
90. Lindblom, L.; Owen, B.J.; Morsink, S.M. Gravitational radiation instability in hot young neutron stars. *Phys. Rev. Lett.* **1998**, *80*, 4843–4846.
91. Andersson, N.; Kokkotas, K.D. The R mode instability in rotating neutron stars. *Int. J. Mod. Phys. D* **2001**, *10*, 381–441.
92. Kolomeitsev, E.E.; Voskresensky, D.N. Mechanism of r-mode stability in young rapidly rotating pulsars. *Eur. Phys. J. A* **2014**, *50*, 180.

93. Kolomeitsev, E.E.; Voskresensky, D.N. Viscosity of neutron star matter and  $r$ -modes in rotating pulsars. *Phys. Rev. C* **2015**, *91*, 025805.
94. Shternin, P.S.; Yakovlev, D.G. Electron-muon heat conduction in neutron star cores via the exchange of transverse plasmons. *Phys. Rev. D* **2007**, *75*, 103004.



© 2018 by the authors. Licensee MDPI, Basel, Switzerland. This article is an open access article distributed under the terms and conditions of the Creative Commons Attribution (CC BY) license (<http://creativecommons.org/licenses/by/4.0/>).